



HAL
open science

Inelastic Compaction in High-Porosity Limestone Monitored Using Acoustic Emissions

Patrick Baud, Alexandre Schubnel, Michael Heap, Alexandra Rolland

► **To cite this version:**

Patrick Baud, Alexandre Schubnel, Michael Heap, Alexandra Rolland. Inelastic Compaction in High-Porosity Limestone Monitored Using Acoustic Emissions. *Journal of Geophysical Research: Solid Earth*, 2017, 122 (12), pp.9989 - 10,008. 10.1002/2017JB014627 . hal-01789361

HAL Id: hal-01789361

<https://hal.science/hal-01789361>

Submitted on 11 Jan 2021

HAL is a multi-disciplinary open access archive for the deposit and dissemination of scientific research documents, whether they are published or not. The documents may come from teaching and research institutions in France or abroad, or from public or private research centers.

L'archive ouverte pluridisciplinaire **HAL**, est destinée au dépôt et à la diffusion de documents scientifiques de niveau recherche, publiés ou non, émanant des établissements d'enseignement et de recherche français ou étrangers, des laboratoires publics ou privés.

RESEARCH ARTICLE

10.1002/2017JB014627

Special Section:

Seismic and Micro-Seismic
Signature of Fluids in Rocks:
Bridging the Scale Gap

Key Points:

- Presence of significant quartz (20 wt. %) did not impact the mechanical behavior of Saint-Maximin limestone (porosity 37%)
- Inelastic compaction in Saint-Maximin limestone was accompanied by abundant acoustic emission (AE) activity, capturing strain localization
- Microcracking reduced P wave velocity near the yield point, while porosity reduction resulted in a significant increase in P wave velocity

Supporting Information:

- Supporting Information S1
- Figure S1

Correspondence to:

P. Baud,
patrick.baud@unistra.fr

Citation:

Baud, P., Schubnel, A., Heap, M., & Rolland, A. (2017). Inelastic compaction in high-porosity limestone monitored using acoustic emissions. *Journal of Geophysical Research: Solid Earth*, 122, 9989–10,008. <https://doi.org/10.1002/2017JB014627>

Received 29 JUN 2017

Accepted 1 DEC 2017

Accepted article online 13 DEC 2017

Published online 29 DEC 2017

Inelastic Compaction in High-Porosity Limestone Monitored Using Acoustic Emissions

Patrick Baud¹ , Alexandre Schubnel², Michael Heap¹ , and Alexandra Rolland¹¹Institut de Physique du Globe de Strasbourg, UMR 7516 CNRS, Université de Strasbourg/EOST, Strasbourg, France,²Laboratoire de Géologie, CNRS UMR 8538, Ecole Normale Supérieure, Paris, France

Abstract We performed a systematic investigation of mechanical compaction and strain localization in Saint-Maximin limestone, a quartz-rich, high-porosity (37%) limestone from France. Our new data show that the presence of a significant proportion of secondary mineral (i.e., quartz) did not impact the mechanical strength of the limestone in both the brittle faulting and cataclastic flow regimes, but that the presence of water exerted a significant weakening effect. In contrast to previously published studies on deformation in limestones, inelastic compaction in Saint-Maximin limestone was accompanied by abundant acoustic emission (AE) activity. The location of AE hypocenters during triaxial experiments revealed the presence of compaction localization. Two failure modes were identified in agreement with microstructural analysis and X-ray computed tomography imaging: compactive shear bands developed at low confinement and complex diffuse compaction bands formed at higher confinement. Microstructural observations on deformed samples suggest that the recorded AE activity associated with inelastic compaction, unusual for a porous limestone, could have been due to microcracking at the quartz grain interfaces. Similar to published data on high-porosity macroporous limestones, the crushing of calcite grains was the dominant micromechanism of inelastic compaction in Saint-Maximin limestone. New P wave velocity data show that the effect of microcracking was dominant near the yield point and resulted in a decrease in P wave velocity, while porosity reduction resulted in a significant increase in P wave velocity beyond a few percent of plastic volumetric strain. These new data highlight the complex interplay between mineralogy, rock microstructure, and strain localization in porous rocks.

1. Introduction

An understanding of the short- and long-term evolution of reservoirs and aquifers hinges upon a fundamental understanding of inelastic compaction of porous rocks and its implications on fluid flow at various scales. In the past few decades, experimental rock mechanics studies have considerably improved our understanding of the micromechanism of inelastic compaction operative in situ in porous sedimentary formations and of the associated failure modes to be expected in various geophysical environments (see Wong & Baud, 2012, for a review). Although inelastic compaction occurs only by grain crushing and pore collapse in porous sandstone (Zhang, Wong, & Davis, 1990), a great variety of mechanisms such as pore collapse (Zhu, Baud, & Wong, 2010) and grain crushing (Brantut et al., 2014a), but also crystal plasticity (Griggs, Turner, & Heard, 1960; Nicolas et al., 2016; Turner, Griggs, & Heard, 1954) and pressure-solution (Croizé, Renard, & Gratier, 2013), can potentially play an important role in more complex porous sedimentary rocks, such as limestones. In porous rocks, three failure modes associated with inelastic compaction were observed in the laboratory: compactive shear bands (Bésuelle, 2001; Bésuelle, Baud, & Wong, 2003; Charalampidou et al., 2014; Ji et al., 2015), compaction bands (Baud, Klein, & Wong, 2004; Baud, Meredith, & Townend, 2012; Cilona et al., 2014), and homogeneous cataclastic flow (Menéndez, Zhu & Wong, 1996; Vajdova et al., 2012). Several field studies on sandstone (Aydin, Borja, & Eichhubl, 2006; Eichhubl, Hooker, & Laubach, 2010; Mollema & Antonellini, 1996) and carbonate (Rath et al., 2011; Rotevatn et al., 2016; Rustichelli et al., 2012; Tondi et al., 2006) formations have characterized the geometric attributes of and the complex interplay between compactive shear bands and compaction bands.

In the laboratory, studying strain localization in carbonates has proved more challenging than in sandstones, for several reasons. First, the complexities of the compactant failure mode in deformed limestones can be concealed by mineralogical homogeneity (i.e., pure limestones containing close to 100 wt % calcite), unlike in sandstones (see, e.g., Fortin, Schubnel, & Guéguen, 2005). Second, acoustic emissions (AE)—high-

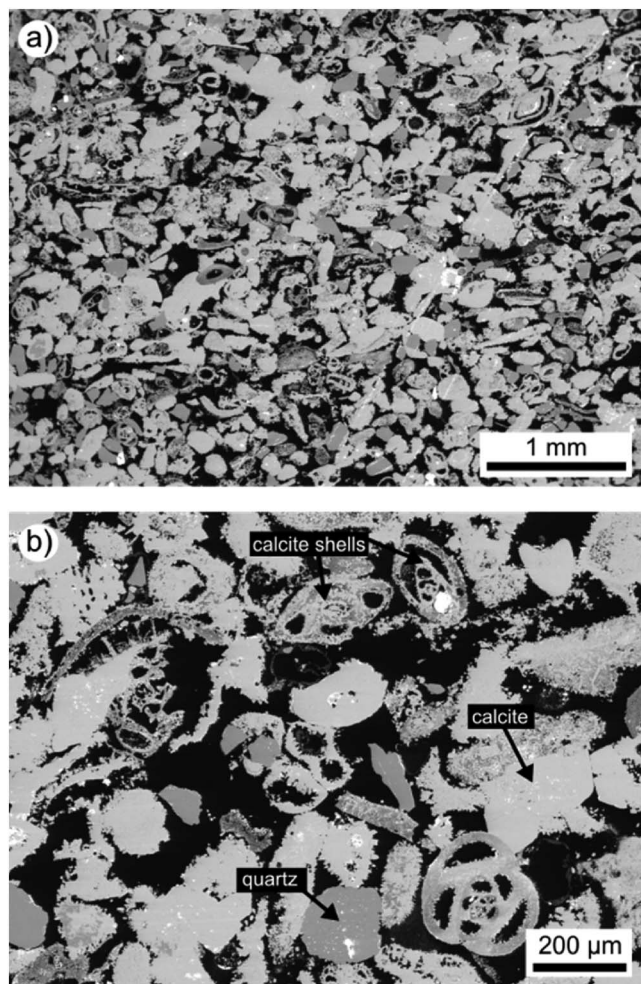


Figure 1. (a and b) Backscattered SEM images of intact Saint-Maximin limestone. The componentry is labeled in Figure 1b: subrounded calcite grains (~250 μm in diameter), subrounded quartz grains (~150 μm in diameter), and calcite fossil shells containing both microporosity and macroporosity (~150 μm in diameter).

frequency elastic wave packets generated by the rapid release of strain energy such as during microcracking—have been used as a powerful diagnostic tool in laboratory deformation studies on sandstones. They have been used to monitor and record damage in real time during the approach to and formation of shear fractures (Lockner, 1993) and compaction bands (Fortin et al., 2006; Townend et al., 2008; Heap et al., 2015). In contrast, and to our knowledge, most existing laboratory studies did not report any significant AE activity during deformation and failure of carbonates (see, e.g., Baud, Schubnel, & Wong, 2000; Vajdova, Baud, & Wong, 2004). Schubnel et al. (2006), for example, recorded 1.5 orders of magnitude less AE during failure of Carrara marble than for Fontainebleau sandstone. The extent to which AE can be used to monitor inelastic compaction in carbonates therefore remains unclear. To date, the analysis of complex failure modes in high-porosity carbonates has relied only on laborious microstructural analysis (Vajdova et al., 2010, 2012) and X-ray computed tomography (CT) (Ji et al., 2012, 2015) performed post mortem on deformed samples.

In this study, we investigated systematically the possibility of monitoring inelastic compaction in a high-porosity limestone using AE. We chose Saint-Maximin limestone (called SML herein) from the Paris Basin in France mainly because a previous study revealed that compaction localization occurs in this rock under a wide range of laboratory conditions (Baud et al., 2009). Our first objective was to therefore investigate whether AE monitoring of stress-induced damage could be performed in SML and if this would help our understanding of compaction localization in carbonates.

Carbonate rocks are widely recognized to have microstructure, and in particular pore structure, that is significantly more complex than siliciclastic rocks (Choquette & Pray, 1970; Folk, 1980; Lucia, 1995). Hence, pilot laboratory studies mostly selected relatively pure carbonates (i.e., close to 100 wt % calcite) and focused on somehow simpler end-members such as micritic (Nicolas et al., 2016; Vajdova et al., 2010), allochemical (Dautriat et al., 2011; Vajdova et al., 2012), microporous (Regnet et al., 2015; Baud et al., 2016), or macroporous limestones (Baud et al., 2017). The question of the impact of the composition and in particular the presence of secondary minerals (such as quartz

or dolomite) on the strength and rheology of high-porosity limestone has so far remained understudied, although high-pressure, high-temperature torsion experiments on low-porosity synthetic limestones have shown that the addition of dolomite (Delle Piane, Burlini, & Kunze, 2009; Kushnir et al., 2015) or quartz (Rybacki et al., 2003) serves to increase the strength of limestone. Another study found that the strength of an iron-rich oolitic limestone (containing oolites of concentric layers of goethite, calcite bioclasts, and a cement comprising calcite, siderite, magnesite, iron oxides, and berthierine) was reduced following the oxidation of the iron-bearing mineral constituents (Grgic, Giraud, & Auvray, 2013). Since SML contains a significant proportion of quartz (Baud et al., 2009), the second objective of this study was to quantify how the presence of a significant quartz phase would influence the strength of a high-porosity limestone over a wide range of pressures.

Mechanical compaction and strain localization could potentially significantly affect elastic wave velocities in a porous medium. Most experimental studies at high pressure have focused so far on sandstones (Ayling, Meredith, & Murrell, 1995; Fortin, Schubnel, & Guéguen, 2007). Fortin et al. (2007), for example, showed that the onset of inelastic compaction triggered a decrease in both P and S wave velocities in Bleurswiller sandstone (25% porosity). This perhaps counterintuitive result—since decreases in porosity are typically associated with increases in elastic wave velocity—was interpreted as the impact of newly formed cracks produced by grain crushing that played a dominant role on the evolution of elastic wave velocities. There

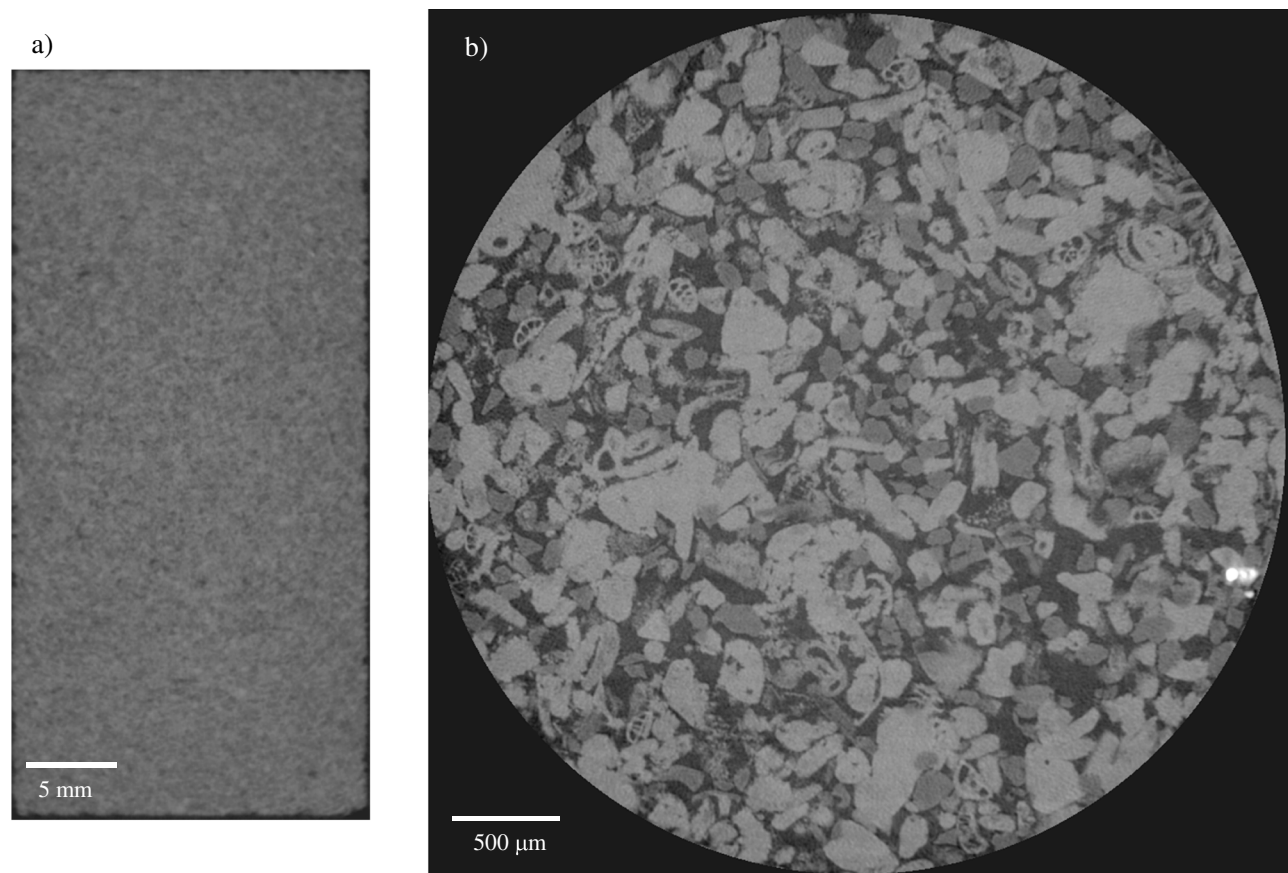


Figure 2. (a and b) Micro-CT data on the same intact sample of SML with resolution 40 μm (Figure 2a) and 4 μm (Figure 2b).

is a paucity of data of this nature on high-porosity limestones. Our third and final objective was therefore to study the evolution of P wave velocities during the inelastic compaction of SML.

2. The Studied Limestone and Experimental Methods

2.1. Material Description

Saint-Maximin limestone from the Lutetian age, a major building stone from the center of the Paris Basin, was selected for this study due to its high porosity and quartz content (Fronteau et al., 2010). Our blocks were taken from the Rocamat quarry in Saint-Maximin-sur-Oise, north of Paris, France. These blocks are considered similar to the one used in a previous study by Baud et al. (2009). Intact SML contains three components: subrounded dense (i.e., no microporosity) calcite grains (~ 250 μm in diameter), subrounded quartz grains (~ 50 – 100 μm in diameter), and calcite fossil shells (~ 150 μm in diameter) containing both microporosity and macroporosity (Figure 1a). SML is a grain-supported carbonate rock devoid of a micritic or sparry cement (Figure 1). X-ray diffraction analysis gave a nominal composition of ~ 80 wt % calcite and ~ 20 wt % quartz for the block used in this study. X-ray microtomography (μCT) imaging was performed on an intact sample of SML at the High-Resolution CT Facility at the University of Texas at Austin, following the procedures detailed by Ketcham and Carlson (2001) and Louis et al. (2006). Figure 2a presents CT data obtained on the whole sample (2 cm diameter and 4 cm length) at a voxel size resolution of 40 μm . At the sample scale, SML appears quite homogeneous with no visible heterogeneity due to bedding or laminations (Figure 2a). At higher voxel size resolution (4 μm), μCT data revealed some complex macropore shapes in intact SML (Figure 2b). Mercury porosimetry data presented by Baud et al. (2009) show that a large proportion of pore throat diameters in intact SML are larger than 20 μm .

2.2. Experimental Methodology for Deformation Experiments

The mechanical behavior of SML in nominally dry conditions (i.e., samples dried in a vacuum oven at 40°C for at least 48 h) was systematically studied by Baud et al. (2009). In this study, we performed two series of dry and wet (i.e., sample vacuum saturated with deionized water) experiments. Eighteen new experiments were performed at Ecole et Observatoire des Sciences de la Terre (EOST) Strasbourg (France), and six new experiments were performed at ENS Paris (France) for acoustic monitoring. Two sets of cylindrical samples were therefore cored orthogonal to the macroscopic sedimentary bedding: 20 mm in diameter and 40 mm in length for the experiments performed in Strasbourg and 38.2 mm in diameter and 84 mm in length for the experiments performed at ENS Paris. In both cases, samples were dried in vacuo at 40°C for a minimum of 48 h and then saturated with deionized water. Porosity was then measured by water imbibition and the triple weight technique (Ulusay & Hudson, 2007). We found an average connected porosity of 37%. Connected porosity was also measured on selected samples using a helium pycnometer and gave values of porosity within 1% of our triple weight porosities.

The procedure for triaxial experiments in Strasbourg was described in detail by Baud et al. (2015) and Farquharson, Baud, and Heap (2017). Jacketed samples were deformed at a nominal strain rate of $10^{-5}/s$ at confining pressures ranging from 3 to 120 MPa. A computer controlled stepping motor connected to a pressure transducer regulated the confining pressure with an accuracy of 0.05 MPa. The axial load was applied by a piston controlled by a second computer-controlled stepping motor. Axial displacement was measured outside the pressure vessel with a capacitive transducer with accuracy 0.2 μm mounted on the moving piston and servo-controlled at a fixed rate (corresponding to a nominal strain rate of $10^{-5}/s$). Wet experiments were performed under fully drained conditions, ensured by the high permeability of SML of $5.5 \times 10^{-13} m^2$ (measured under a confining pressure of 1 MPa; Farquharson et al., 2015), at a fixed pore fluid (deionized water) pressure of 10 MPa. The pore volume change was recorded by monitoring the displacement of the pore pressure generator with an angular encoder. The porosity change was calculated from the ratio of the pore volume change to the initial bulk volume of the sample. For dry experiments, volumetric strain was recorded by monitoring the piston displacement of the confining pressure generator with an angular encoder (Baud et al., 2009). The output of AE energy (the area under the received AE waveform) during deformation was recorded using a piezoelectric crystal attached to the top of the upper piston and a single-channel AE node (from physical acoustics).

Two hydrostatic (dry and wet) and four triaxial constant strain rate experiments, two dry and two wet, were performed at ENS Paris following the same procedure used by Wang et al. (2013). The triaxial tests were performed at a constant strain rate of $4 \times 10^{-6}/s$. Axial and radial strains were measured using four strain gauges glued on the surface of each sample. Axial strain was also measured with three external Foucault current sensors. Sixteen *P* wave piezoelectric ceramic transducers (PI ceramic PI255, 0.5 MHz resonance frequency) were glued directly on each sample with a specific pattern enabling longitudinal, normal, and tilted measurements (with respect to the major principal stress). The transducers were positioned with 0.5 mm accuracy and were used in both active mode and passive mode. Inside the vessel, the sample was covered with a neoprene jacket, which insulated it from the confining oil. Acoustic waveforms were amplified at 40 dB and recorded at 10 MHz sampling rate using a Richter system (Itasca Ltd.). A complete description of the acoustic system is given in Ougier-Simonin et al. (2011) and Wang et al. (2013). A classical ultrasonic pulse transmission technique was used for *P* wave velocity measurements. Independent velocity measurements were measured along three different angles with respect to the vertical: *Vp0* along the horizontal path, perpendicular to the compression axis; *Vp34*; and *Vp54* along two diagonal paths, respectively, inclined at 34 and 54° from the horizontal plane. For each measurement, 10 waveforms were stacked in order to increase the signal/noise ratio. Note that only raypaths going through the center of the specimen were used except when explicitly stated; otherwise, velocity measurements presented in the following are sample average along those paths. Arrival times were determined using cross correlations, and relative error on velocity measurements is about 1%. In passive mode, transducers were used to record the output of AE. A trigger logic was applied, generally set at 150 mV on three channels within a 10 μs window. AE time arrivals were autopicked. Hypocenter locations were determined using a collapsing grid search algorithm, assuming an evolving either isotropic (hydrostatic experiments) or transversely isotropic (triaxial experiments) homogeneous *P* wave velocity profile within the sample. A complete description of the technique is given in Ougier-Simonin et al. (2011). The total number of AE recorded being significant, up to 3.10^4 , we only show AEs that were

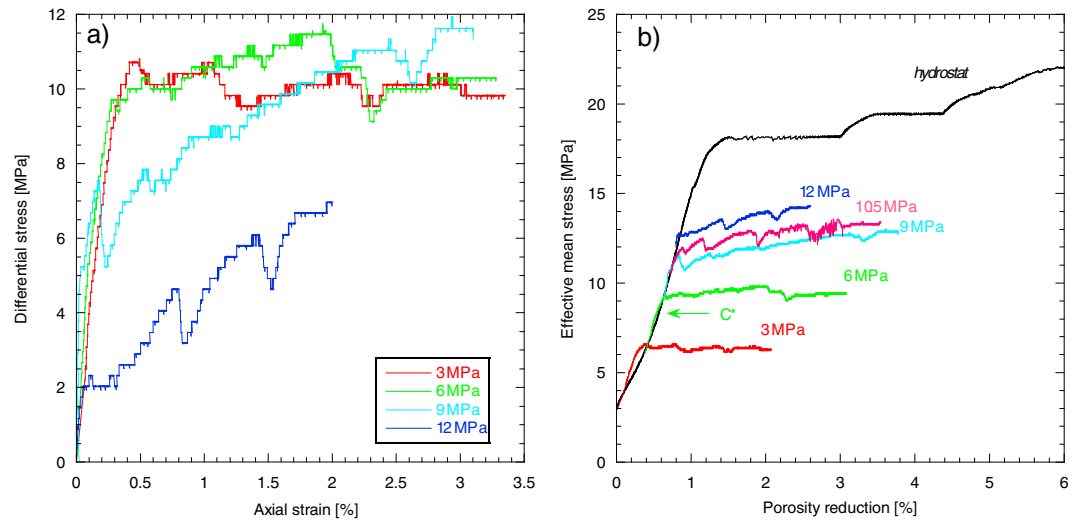


Figure 3. Mechanical data for triaxial compression experiments on water-saturated SML. (a) Differential stress as a function of axial strain. (b) Porosity reduction as a function of effective mean stress.

accurately located by seven stations at least, with average time residuals between the picked and calculated of 0.5 μ s or less. For these, using a *P* wave velocity of 3,500 m/s, we consider that AE hypocenter location errors were, on average, on the order of ± 2 mm.

In wet experiments, pore fluid was introduced into the sample through hardened steel end pieces placed on the top and bottom of the rock sample.

3. Mechanical Data

In this paper we used the convention that the compressive stresses and compactive strains (i.e., shortening and porosity decrease) are considered to be positive. The maximum and minimum (compressive) principal stresses were denoted by σ_1 and σ_3 , respectively. The pore pressure was denoted by P_p , and the difference $P_c - P_p$ between the confining pressure ($P_c = \sigma_2 = \sigma_3$) and pore pressure was referred to as the “effective

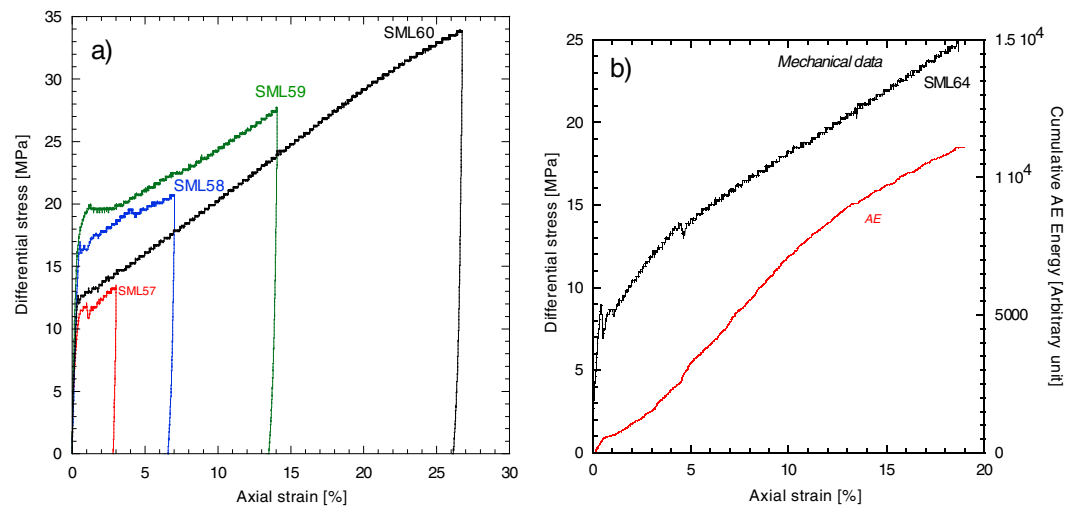


Figure 4. Mechanical data for samples deformed at the same confining pressure of 9 MPa to different level of axial strain for microstructural analysis. The names of the samples are indicated next to the curves. (a) Differential stress as a function of axial strain. (b) Differential stress and cumulative AE activity as a function of axial strain for sample SML64.

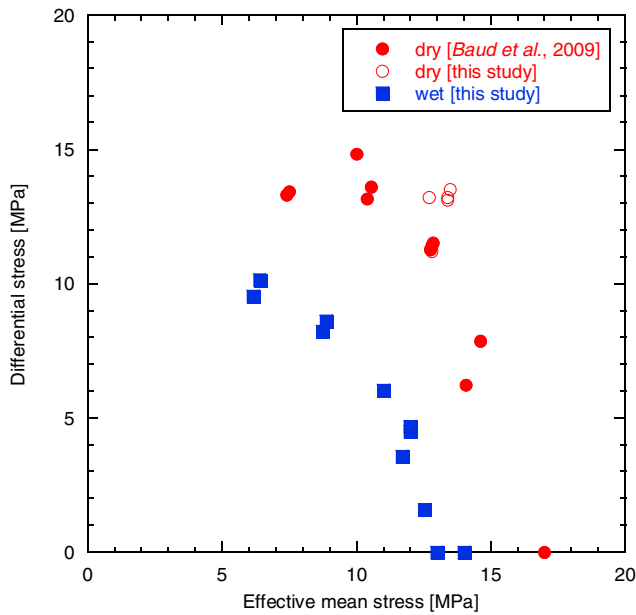


Figure 5. Compactive yield caps for onset of shear-enhanced compaction C^* in the effective mean stress and differential stress space for the dry data of Baud et al. (2009) (red closed circles) and this study (red open circles) and water-saturated (blue squares) SML.

pressure" P_{eff} (i.e., we assume a simple effective pressure law). The effective mean stress $(\sigma_1 + 2\sigma_3)/3 - P_p$ was denoted by P and the differential stress $\sigma_1 - \sigma_3$ by Q .

Figure 3a presents representative new triaxial data on water-saturated SML. These data are qualitatively similar to the published dry data presented on the same rock by Baud et al. (2009) and essentially show two different mechanical behaviors. At 3 and 6 MPa of effective pressure, a plateau in the mechanical data was visible beyond the yield point. This behavior is usually associated with a transitional regime between brittle and ductile behavior (Baud, Vajdova, & Wong, 2006) and was shown to involve compactive shear bands (Bésuelle et al., 2003). At 9 MPa of effective pressure and above, significant strain hardening was observed in the mechanical data. At all tested pressures, the mechanical data were punctuated by episodic stress drops that reached an amplitude of 1 MPa at the highest tested pressure. These stress drops are usually an indicator of compaction localization (see, e.g., Baud et al., 2004). However, visual inspection of the samples did not reveal any clear failure mode on the surface of the deformed samples of SML. Figure 3b shows that all samples failed by shear-enhanced compaction starting from a critical state of stress usually denoted as C^* (Wong, David, & Zhu, 1997), the point whereat the deviatoric part of the loading resulted in an acceleration of compaction. The reference hydrostat taken from the earlier study of Baud et al. (2009) showed that the onset of inelastic compaction under hydrostatic compaction (denoted P^*) occurred at

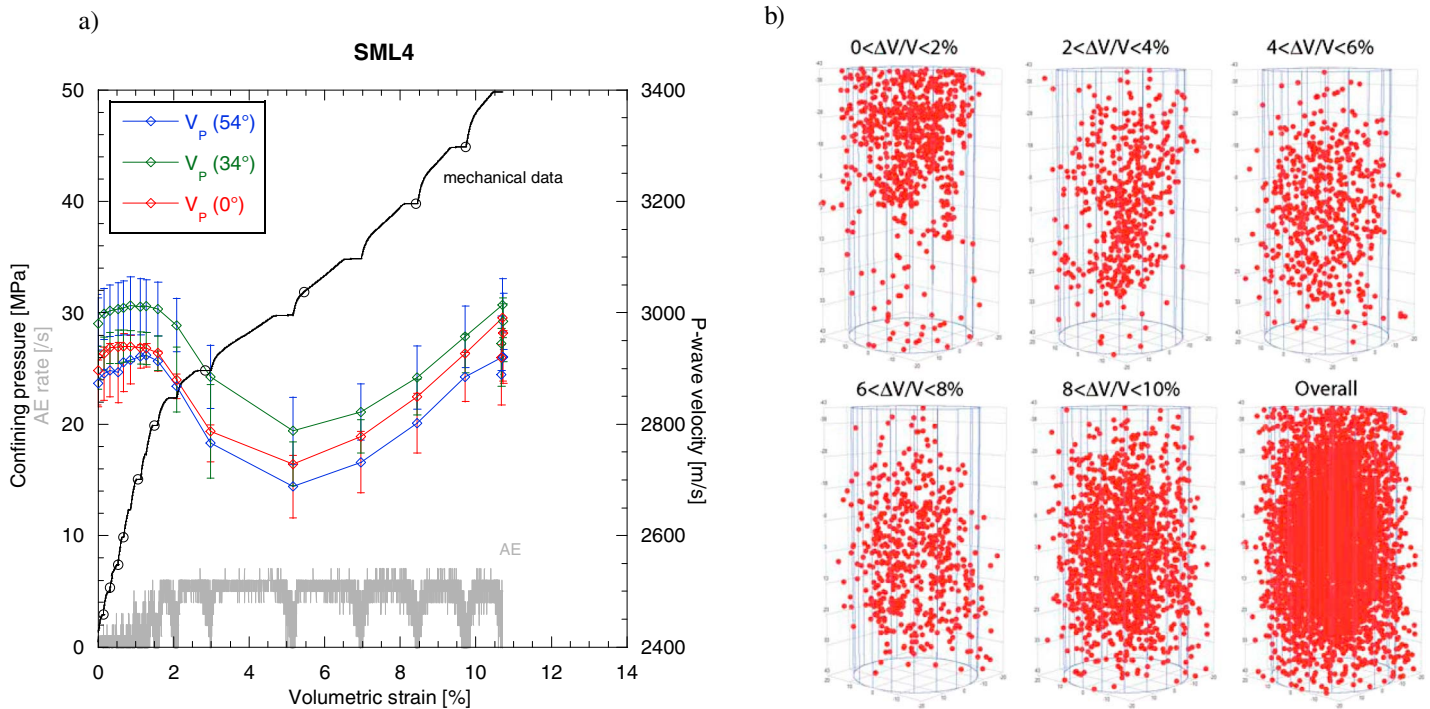


Figure 6. Data on sample SML4 deformed hydrostatically in dry conditions. (a) Confining pressure (black), AE rate (gray), and P wave velocity as a function of volumetric strain. P wave velocity was measured on horizontal paths (0° , red) and on two other paths oriented at 34° (green) and 54° (blue) with respect to the horizontal. The confining pressure was increased by small steps in this experiment. The end of each step corresponded to the open circles in the mechanical data. (b) AE hypocenter distribution for different intervals of volumetric strain.

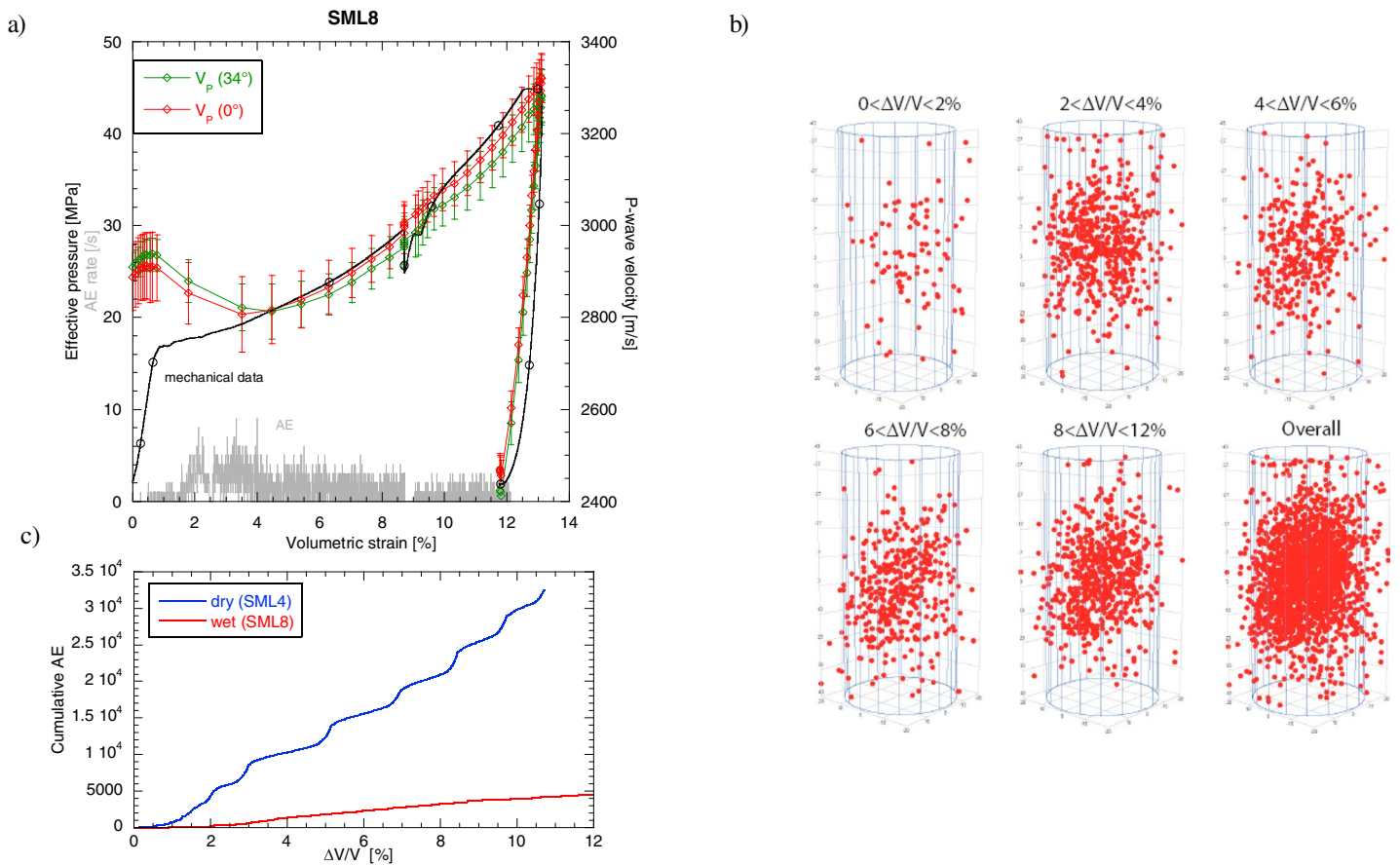


Figure 7. Data on sample SML8 deformed hydrostatically in wet conditions. (a) Effective pressure (black), AE rate (gray) and P wave velocity measured as a function of volumetric strain. P wave velocity was measured on horizontal paths (0° , red) and on another path oriented at 34° (green) with respect to the horizontal. (b) AE hypocenter distribution for different intervals of volumetric strain. (c) Cumulative AE hits as a function of volumetric for samples SML4 and SML8 deformed hydrostatically under dry and wet conditions, respectively.

13 MPa of effective pressure. At the highest tested pressures, we noted that the porosity change versus axial strain curves had almost a slope of unity beyond C^* , showing that inelastic compaction occurred with almost no radial strain.

Five additional triaxial experiments were performed in dry conditions at the same confining pressure of 9 MPa for microstructural analysis to complete previous observations presented on SML by Baud et al. (2009). The data compiled in Figure 4 reveal two important aspects of inelastic compaction in SML. First, we observed significant variability in the strength of SML in samples deformed in the same conditions (Figure 4a). Second, the inelastic compaction of SML was associated with significant AE activity (Figure 4b). The cumulative AE energy (area of the negative part of the received waveforms) presented in Figure 4b corresponds to more than 14,000 AE hits recorded in a sample deformed to 19% axial strain. The AE activity started around C^* and increased exponentially up to about 13% of axial strain; beyond this point the AE energy rate decreased (Figure 4b).

Figure 5 compiles our new data and published data on dry and wet SML in a plot of differential stress (Q) as a function of the effective mean stress (P). The critical pressures P^* and C^* are presented in P - Q stress space. These data are also summarized in Table S1 in the supporting information. Figure 5 shows that the presence of water induced significant weakening in SML (i.e., the onset of C^* at a given effective pressure was reduced when the samples were wet). A weakening effect of water on limestone was also reported by Lisabeth and Zhu (2015) and Nicolas et al. (2016). Baud et al. (2009) interpreted the measured weakening on SML using the micromechanical model previously used to model stress-induced grain crushing (Zhang et al., 1990).

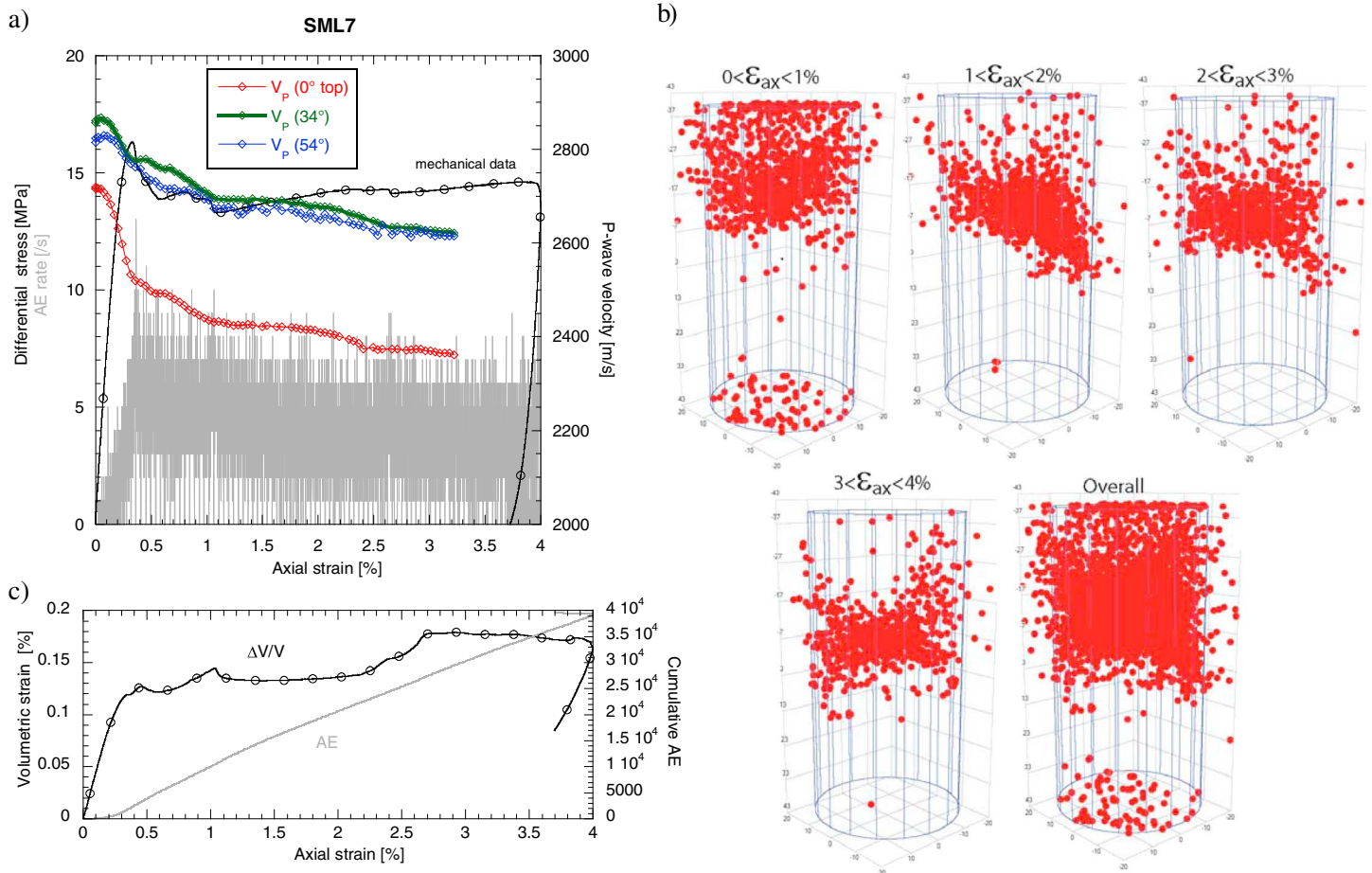


Figure 8. Data on sample SML7 deformed triaxially in dry conditions at a confining pressure of 3 MPa. (a) Confining pressure (black), AE rate (gray), and P wave velocity as a function of volumetric strain. P wave velocity was measured on a horizontal path in the top of the sample (0° , red) and on two other paths oriented at 34° (green) and 54° (blue) with respect to the horizontal. (b) AE hypocenter distribution for different intervals of volumetric strain. (c) Volumetric strain (black) and cumulative AE (gray) as a function of axial strain. Major principal stress was vertical.

Baud et al. (2009) concluded that the strength reduction was likely a result of the reduction of the fracture toughness of calcite in the presence of water.

Based on these results, six experiments dedicated to the study of AE activity in SML were performed on large samples (38.2 mm in diameter and 84 mm in length) at ENS Paris, two hydrostatic tests (dry and wet) and 4 triaxial constant strain rate experiments (two dry and two wet). These new data are compiled in Figures 6–11. Consistent with the results presented in Figure 4b, hydrostatic compaction in dry SML is accompanied by significant AE activity starting at P^* (Figure 6). More than 30,000 events were recorded in about 8 h while the sample was deformed up to 10.5% of volumetric strain (Figure 6a). In this hydrostatic experiment, the confining pressure was increased in a stepwise fashion and this is why the AE rate increased and then decreased during each step (Figure 6a). The AE locations show that damage started from the top end of the sample (Figure 6b). As confining pressure was increased, AE events appeared homogeneously distributed in all the sample volume. This scenario is typical of cataclastic flow, as observed in similar studies on sandstone (see, e.g., Fortin et al., 2009a). The fact that localization did not occur in this sample was confirmed by the P wave velocity data. Figure 6a shows that the evolution of V_p (P wave velocity) in the three different orientations was essentially identical. No significant preexisting microcracking was reported in intact SML by the previous study of Baud et al. (2009) based on hydrostatic data. Indeed, during the first poroelastic part of this dry hydrostatic experiment, V_p did not vary much at all. A significant decrease of V_p started at the pressure corresponding to P^* and reached a minimum (corresponding to a decrease of about 6%) after 4% of volumetric strain. Beyond this level of strain, V_p increased to approximately return to its initial value after 10.5% of

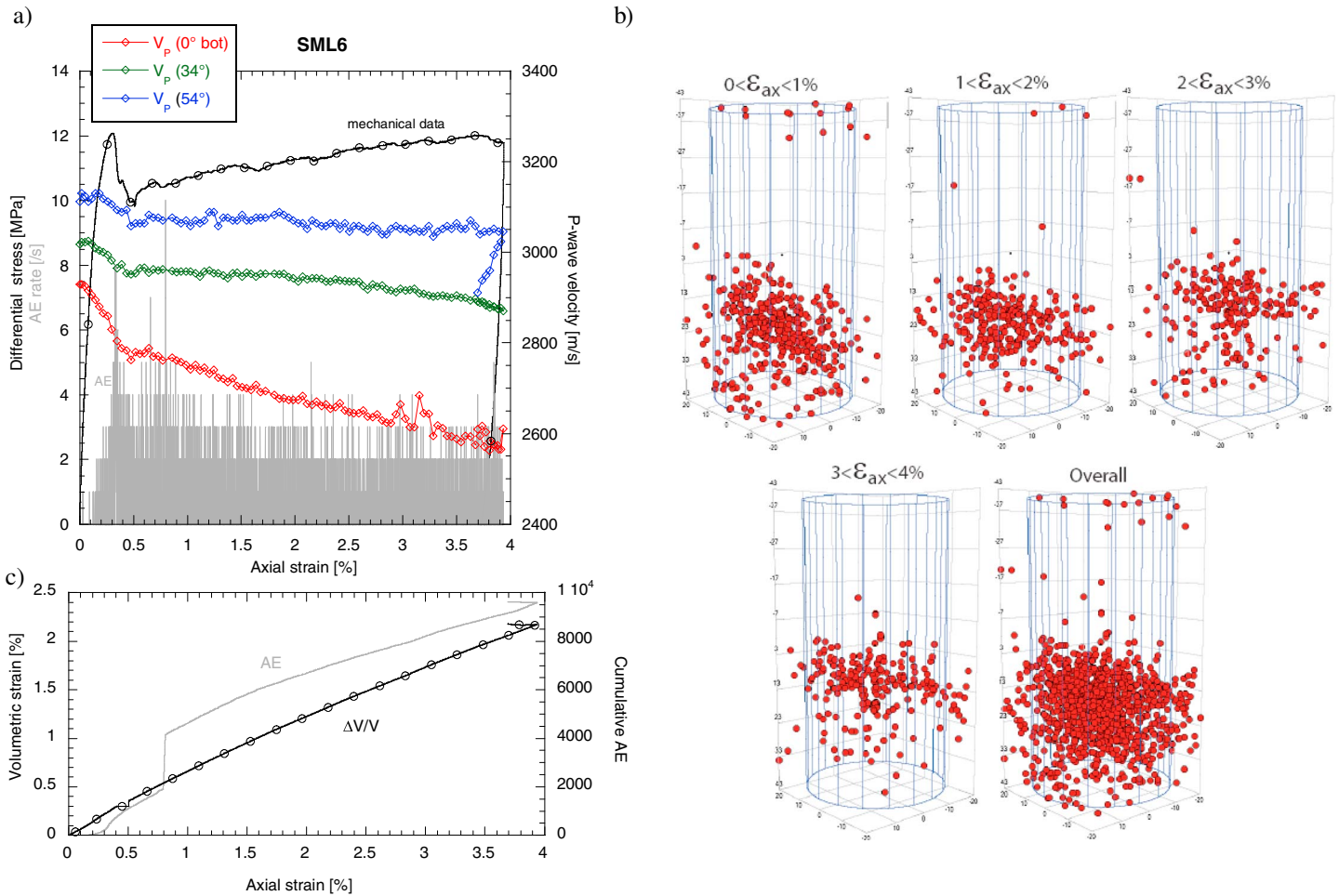


Figure 9. Data on sample SML6 deformed triaxially in wet conditions at an effective pressure of 3 MPa. (a) Effective pressure (black), AE rate (gray), and P wave velocity as a function of volumetric strain. P wave velocity was measured on a horizontal path in the bottom of the sample (0° , red) and on two other paths oriented at 34° (green) and 54° (blue) with respect to the horizontal. (b) AE hypocenter distribution for different intervals of volumetric strain. (c) Volumetric strain (black) and cumulative AE (gray) as a function of axial strain. Major principal stress was vertical.

volumetric strain (Figure 6a). The results of the hydrostatic test in wet conditions were qualitatively similar to the dry data (Figure 7), although the V_p at the end of the experiment had increased to above its initial value at the start of the experiment (Figure 7a). The AE location data show that this wet sample also failed by cataclastic flow (Figure 7b). As shown in Figure 7c, we recorded about 7 times less AE during the hydrostatic experiment performed in wet conditions than in dry conditions. Similar observations were made in low-porosity crystalline rock (see, e.g., Wang et al., 2013). Two mechanisms at least could explain such differences: the increased attenuation in the presence of fluids (since the triggering threshold remained the same in all our experiments) and subcritical crack growth that would radiate less acoustic waves (triaxial creep experiments on sandstone have shown that an increased efficiency of stress corrosion cracking reduces the mechanical work required; i.e., there is an “energy deficit,” to bring a sample to failure; Brantut et al., 2014b). Figure 8 shows the results of a triaxial test performed in dry conditions at 3 MPa of confining pressure. As in the previous tests (Figures 6 and 7), a significant number of AE events were located during this experiment (Figure 8b). The spatial distribution of AE revealed that compaction localization developed in this sample: most of the events occurred in the top half of the sample (Figure 8b). The P wave velocity data are in perfect agreement with the AE locations. V_p decreased slightly with increasing strain when measured in a direction inclined with respect to the major principal stress and a more significant decrease was observed for the horizontal path at the level of the cloud of AE events. Together with the mechanical data (Figure 8a), both AE and V_p data suggest that a compactive shear band developed in this sample. Similar results were obtained on a sample deformed in wet conditions at 3 MPa

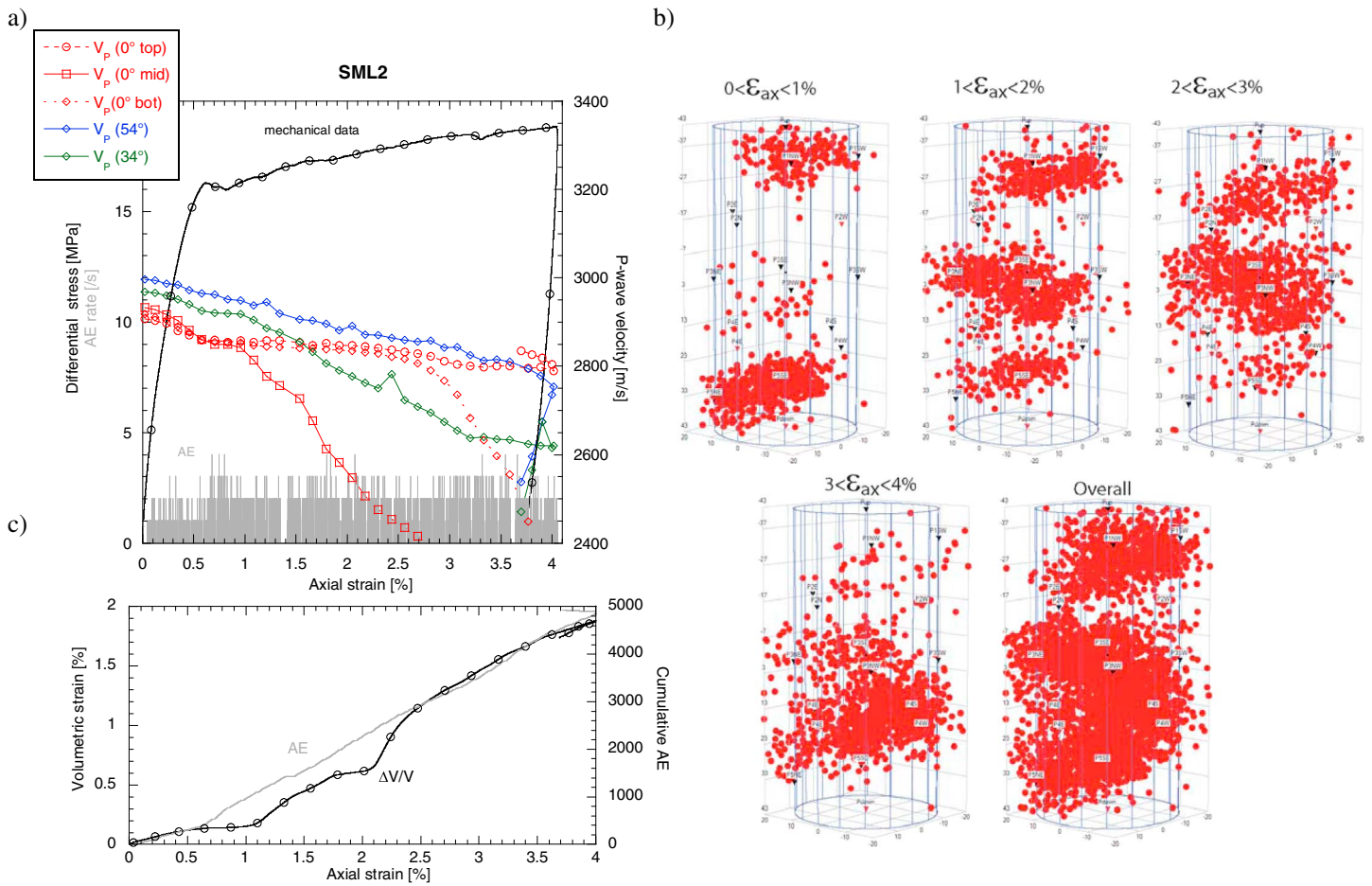


Figure 10. Data on sample SML2 deformed triaxially in dry conditions at a confining pressure of 9 MPa. (a) Confining pressure (black), AE rate (gray), and P wave velocity as a function of volumetric strain. P wave velocity was measured on three horizontal paths (0°) in the top (red circles), middle (red squares), and bottom (red diamonds) of the sample, and on two other paths oriented at 34° (green) and 54° (blue) with respect to the horizontal. (b) AE hypocenter distribution for different intervals of volumetric strain. (c) Volumetric strain (black) and cumulative AE (gray) as a function of axial strain. Major principal stress was vertical.

of effective pressure (Figure 9). Compaction localization also occurred in this sample. In this experiment, most of the AE events occurred in the bottom third of the sample (Figure 9b).

Figure 10 presents the result of a triaxial test performed in dry conditions at a confining pressure of 9 MPa. Five thousand AE events were recorded during this test that lasted 3 h. AE activity was continuous beyond the yield point (Figure 10c). Of all the V_p orientations, the horizontal V_p (0° mid) was affected by stress-induced damage at the lowest axial strain (about 1%) (Figure 10a). Several subhorizontal AE clusters developed successively from the ends to the central part of the sample (Figure 10b).

In wet conditions, the experiment performed at $P_{eff} = 9$ MPa confirmed the significant weakening effect induced by water (Figure 11a). C^* occurred at a differential stress 30% lower than in the dry test shown in Figure 10a. We recorded 2,250 AE events in 3 h (4% axial strain) in this experiment. We observed numerous peaks in AE activity (Figure 11a). Damage started near the top of the sample and moved toward the center as strain increased (Figure 11b). A significant decrease in V_p was observed when the stress-induced damage reached the central part of the sample at about 2.5% strain (Figure 11a).

4. Failure Mode and Microstructural Analysis of Inelastic Compaction

As mentioned above, visual inspection did not reveal any clear failure mode in the deformed samples of SML. Compaction localization was, however, obvious on petrophysical thin sections prepared from a selection of

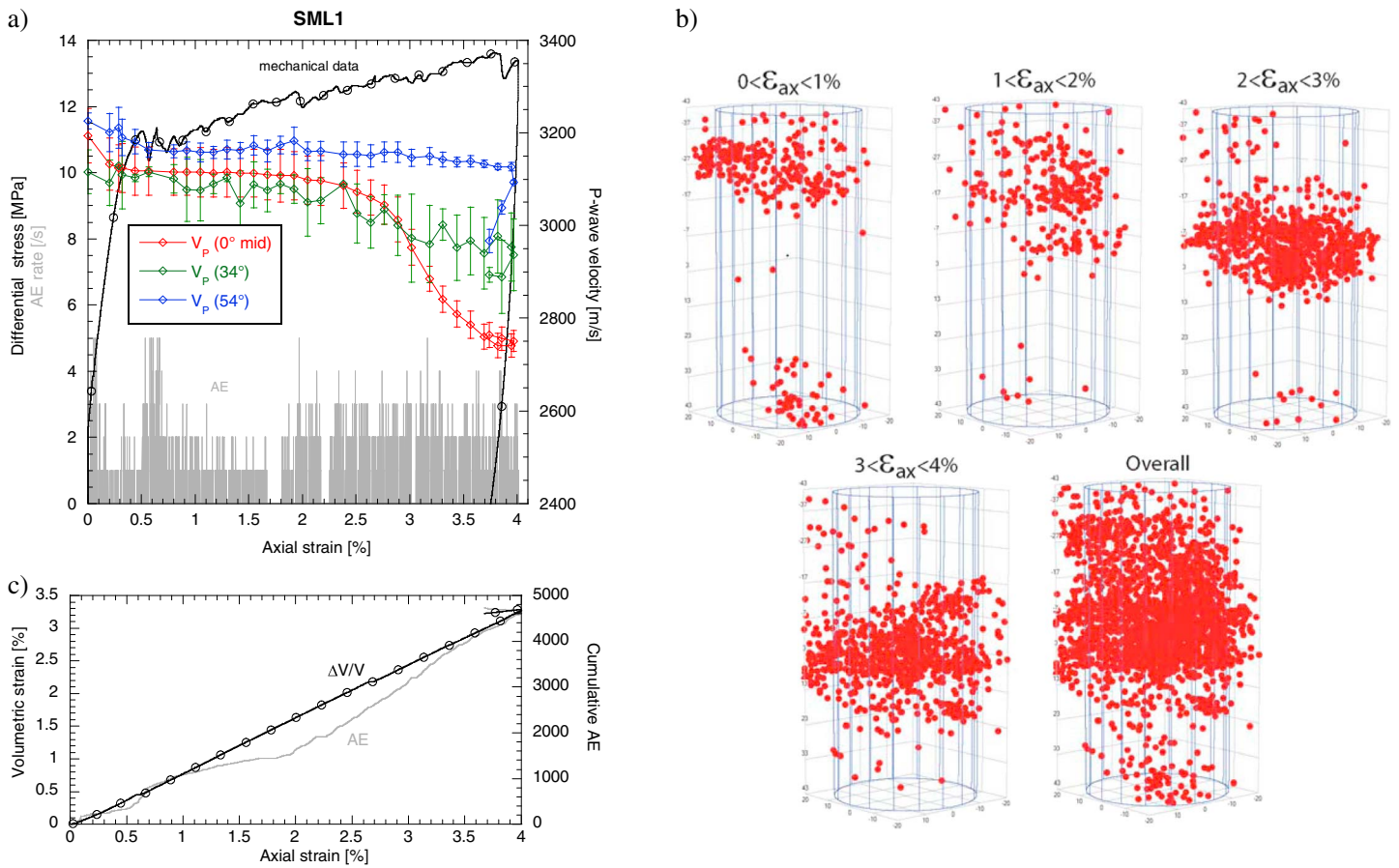


Figure 11. Data on sample SML1 deformed triaxially in wet conditions at an effective pressure of 9 MPa. (a) Effective pressure (black), AE rate (gray), and P wave velocity as a function of volumetric strain. P wave velocity was measured on a horizontal path in the middle of the sample (0° , red) and on two other paths oriented at 34° (green) and 54° (blue) with respect to the horizontal. (b) AE hypocenter distribution for different intervals of volumetric strain. (c) Volumetric strain (black) and cumulative AE (gray) as a function of axial strain. Major principal stress was vertical.

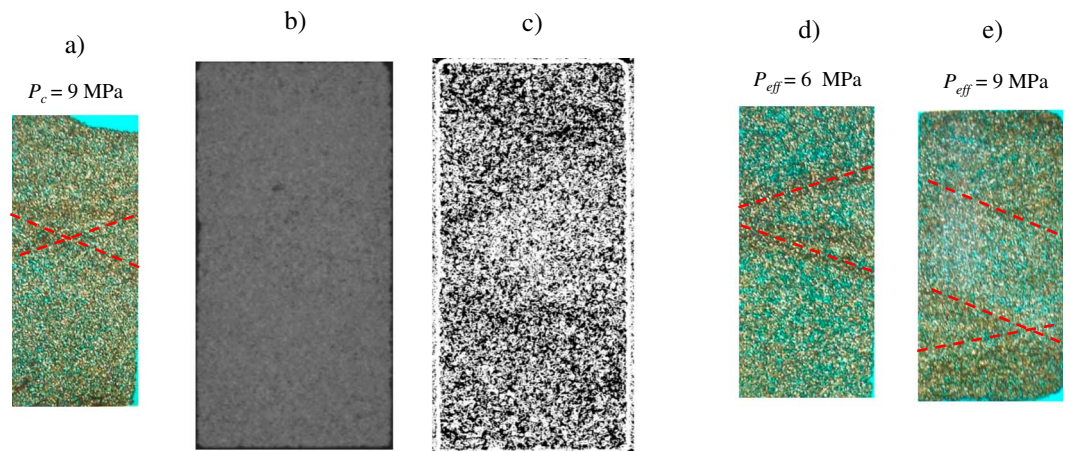


Figure 12. (a) Photograph of a thin section of sample SML27 (Baud et al., 2009) deformed in dry conditions at a confining pressure of 9 MPa. (b) CT data on sample SML37 deformed in dry conditions at a confining pressure of 9 MPa. (c) Spatial distribution of the local coefficient de variation (COV) on a vertical slice. The most damaged zones of the sample are more homogeneous (and smaller standard deviation of the local gray level distribution) and appear darker. Photographs of a thin sections of sample (d) SML18 and (e) SML19 deformed in wet conditions at effective pressures of 6 and 9 MPa, respectively. The red dashed lines in Figures 12a, 12d, and 12e indicate compaction localization. Major principal stress was vertical.

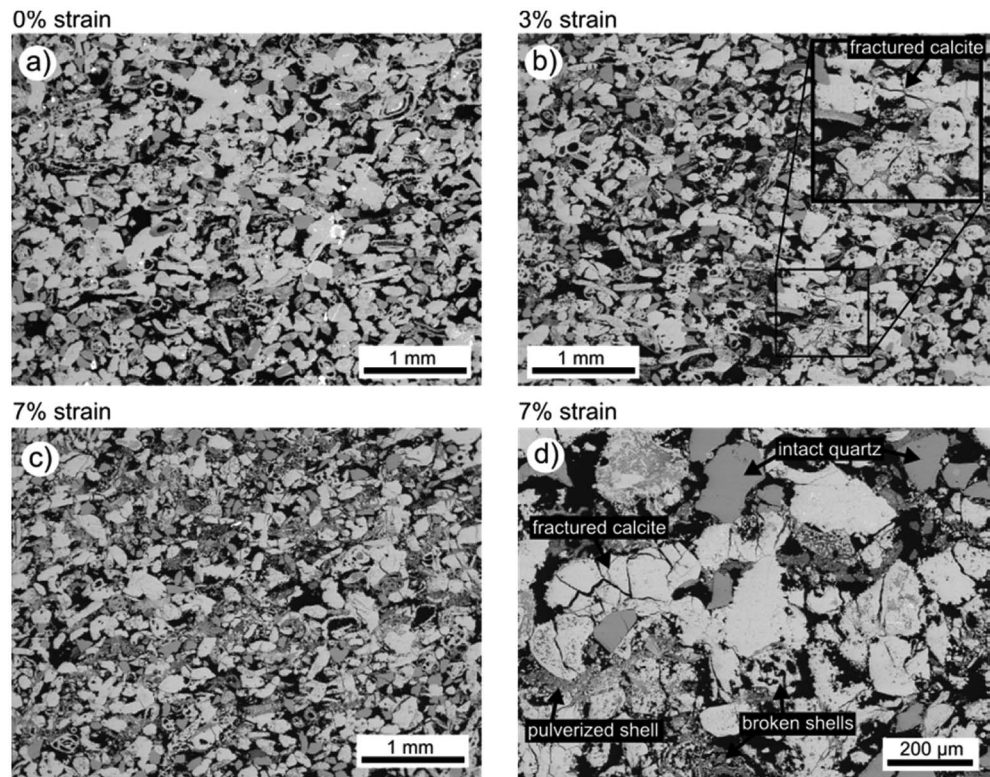


Figure 13. Backscattered SEM images of (a) intact Saint-Maximin limestone and Saint-Maximin limestone deformed to an axial strain of (b) 3% and (c and d) 7%. Inset in Figure 13b shows the Hertzian-type fractures in some of the calcite grains following 3% axial strain. Figure 13d shows the salient deformation microstructures following 7% axial strain: quartz grains remain largely intact, calcite grains are fractured, and fossil shells are either broken or pulverized. Major principal stress was vertical.

samples deformed in Strasbourg in dry and wet conditions. In dry conditions, Baud et al. (2009) showed some complex failure modes involving compactive shear bands and compaction bands. Figure 12a presents one of their samples deformed at a confining pressure of 9 MPa. In an attempt to better map out the localized deformation, we deformed another sample under the same conditions (dry and $P_c = 9$ MPa) and CT imaging was performed using the same resolution as the data shown in Figure 2a. Figure 12b shows a slice of CT data. As it was previously shown in sandstone by Louis et al. (2006), localized compaction did not result in a high enough density contrast to be revealed by CT imaging. However, based on the idea that localized compaction should locally produce a more homogeneous structure, Louis et al. (2006) revealed discrete compaction bands in Diemelstadt sandstone by calculating the local coefficient of variation (COV), the ratio of gray level standard deviation on the mean, determined locally on a small cube with sides of three voxels. Performing this analysis on an SML sample deformed under dry conditions revealed some complex damage patterns at both ends of the samples (Figure 12c). We also found evidence for compaction localization in samples deformed under wet conditions. Figures 12d and 12e show that several compactive shear bands and compaction bands developed in samples deformed at 6 and 9 MPa of effective pressure, respectively.

To provide more insight on the evolution of damage with axial strain, we studied the microstructure of five samples deformed under dry conditions at $P_c = 9$ MPa to 3, 7, 14, and 27% axial strain (Figure 4a). Our microstructural observations show that the sample deformed to 3% strain (Figure 13b) is not dissimilar to the intact sample (Figure 13a). Microcracks can be seen in some calcite grains (see inset in Figure 13b), but the fossil shells and quartz grains appear largely unaffected (Figure 13b). Many more microcracks are present in the calcite grains following deformation to 7% strain (Figures 13c and 13d). We further notice that many of the fossil shells are now broken, or even pulverized (Figures 13c and 13d). However, the quartz grains are

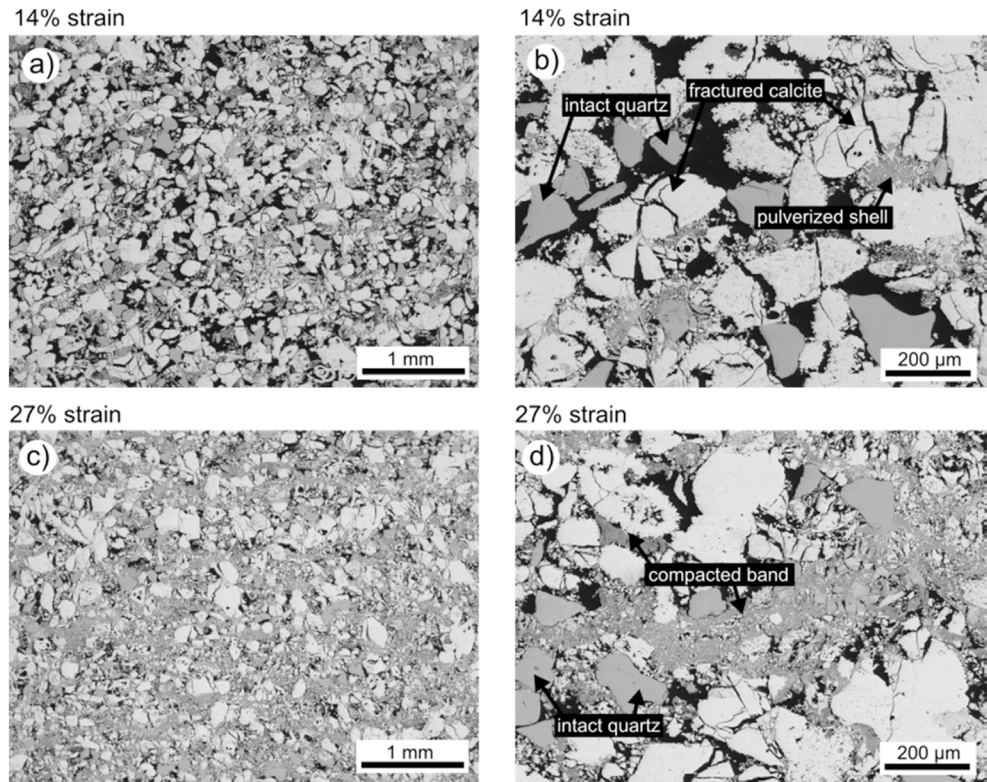


Figure 14. Backscattered SEM images of Saint-Maximin limestone deformed to an axial strain of (a and b) 14% and (c and d) 27%. Figure 14b shows that after 14% axial strain, most calcite grains are broken into two or more angular fragments, the quartz grains remain largely intact, and the fossil shells are nearly all pulverized. Figures 14c and 14d show that the strain appears localized at 27% strain, manifest as discrete bands or lenses of pulverized/crushed material. Major principal stress was vertical.

largely intact (Figures 13c and 13d). The quartz grains are also largely intact when strain was increased to 14% (Figures 14a and 14b), although we note that rare quartz grains are now intensely fractured (Figure 15a). There are many more microcracks in the calcite grains at 14% strain (some grains are even broken into two or more angular fragments; Figures 14a and 14b) and the majority of the fossil shells are completely pulverized into $\sim 1 \mu\text{m}$ fragments (Figures 14a and 14b). The crushing of the calcite grains and fossil shells has resulted in a decrease in sample porosity, as fragmented material occupies space within the voids between the original grains. Following 27% strain, nearly all of the fossil shells have been pulverized

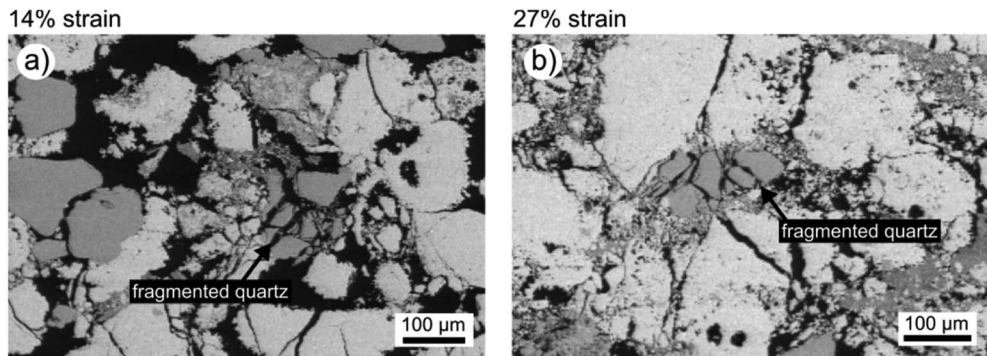


Figure 15. Backscattered SEM images of Saint-Maximin limestone showing fragmented quartz grains. (a) Fragmented quartz grain in a sample deformed to an axial strain of 14%. (b) Fragmented quartz grain in a sample deformed to an axial strain of 27%. Major principal stress was vertical.

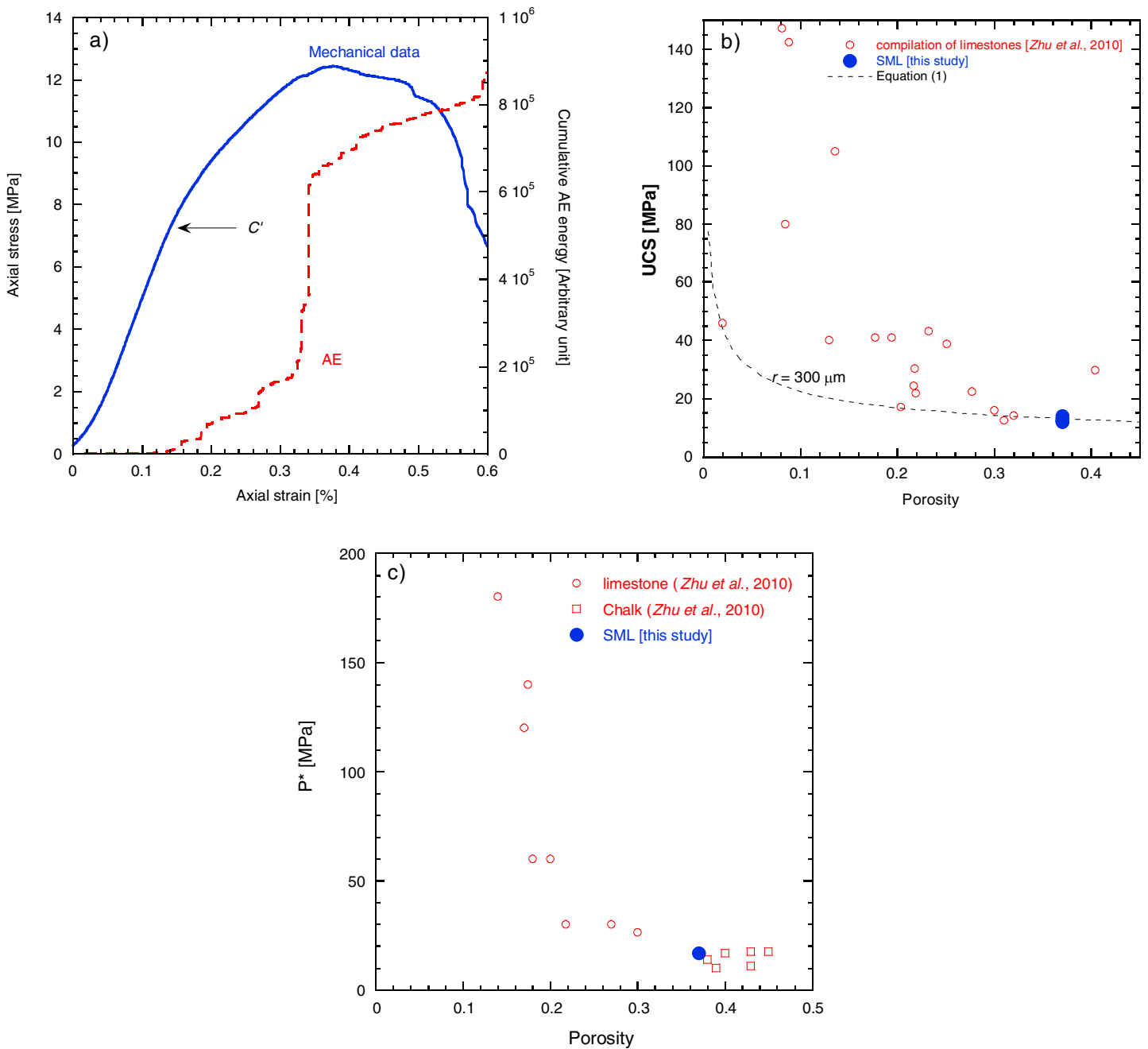


Figure 16. (a) Axial stress (blue line) and cumulative AE energy (red dashed line) as a function of axial strain for an uniaxial experiment performed on a sample of SML. The onset of dilatancy C' is indicated with an arrow. (b) UCS data on porous limestones compiled by Zhu et al. (2010) (red open circles) and SML (solid blue circles) as function of porosity. Theoretical predictions based on the pore-crack model of Sammis and Ashby (1986) are presented as a dashed line for a pore radius $r = 300 \mu\text{m}$ (equation (1)). (c) Onset of inelastic deformation under hydrostatic conditions P^* as a function of porosity for a selection of limestones (open red circles) and chalk (open red squares) compiled by Zhu et al. (2010) and dry SML (solid blue circle).

(Figures 14c and 14d) and majority of calcite grains have been broken into several, if not more, angular fragments, resulting in a grain size reduction that substantially reduced sample porosity (Figures 14c and 14d). A large proportion of quartz grains remained intact, although instances of intensely fractured quartz grains increased from 14% to 27% strain (see example in Figure 15b). We further highlight that there is evidence of compaction localization in the sample deformed to 27% strain. Bands or lenses of broken and pulverized calcite and fossil grains are clearly identifiable; the calcite grains in between these compaction

bands are noticeably more intact (i.e., they are not pulverized but rather broken into two or more angular fragments) (Figures 14c and 14d).

5. Discussion

5.1. Brittle Strength and Inelastic Compaction in SML

One objective of this study was to examine how a large proportion of a secondary mineral, such as quartz, could affect the mechanical strength of a porous carbonate. A previous study has shown, through high-pressure, high-temperature torsion experiments, that an increase in quartz content in low-porosity limestone can increase strength by a factor of 2–5, depending on the temperature and finite strain (Rybacki et al., 2003).

Chemical analysis revealed ~20 wt % of quartz in SML (see section 2.1). Our microstructural analysis suggests that the proportion of quartz varied by up to ~5 wt % from sample to sample. Since no triaxially deformed samples of SML, even at very low confinement, failed by dilatant brittle failure, we performed five additional uniaxial tests to estimate the uniaxial compressive strength (UCS) of dry SML. Figure 16a presents a representative example of the stress-strain data from one of these uniaxial experiments. As expected, the UCS is very low, in the range of 12–13.9 MPa, and brittle failure was accompanied by significant AE activity starting at the onset of dilatancy C' (Figure 16a). In Figure 16b we compare the UCS of SML with the published data on porous carbonates compiled by Zhu et al. (2010). We note that our new data on SML follow the same global trend than the other carbonates: strength is lower when porosity is higher (Figure 16b). A micromechanical interpretation of these results could be obtained by applying the analytical expression derived by Zhu et al. (2010) from Sammis and Ashby's (1986) well-known pore-emanated crack model:

$$\text{UCS} = \frac{1.325 K_{IC}}{\phi^{0.414} \sqrt{\pi r}} \quad (1)$$

where K_{IC} is the fracture toughness and r is the radius of the pores. If we ignore the presence of quartz (justified since we find that the majority of quartz grains remain uncracked following deformation; see Figures 13 and 14) and assume for K_{IC} the value of 0.2 MPa m^{1/2} determined experimentally for calcite by Atkinson and Meredith (1987), we infer a pore radius of 300 μm (Figure 16b), consistent with the larger pores observed in intact SML (Figures 1 and 2). This analysis, coupled with our microstructural observations, suggests that quartz had very little impact on brittle strength of SML. The same conclusion could be reached in the ductile regime. We compared P^* data for SML with published data on porous carbonates and chalk (Figure 16c), and again, SML falls well within the trend defined by the existing data. Our new velocity data suggest that microcracking was significant near the yield point (Figures 6 and 7). Taken together, the microstructural analysis of Baud et al. (2009) and our new microstructural observations (Figures 13–15) show that grain crushing was the main micromechanism of inelastic compaction at the yield point in SML. A recent study made comparable observations in Leitha limestone of porosity between 21 and 31% and also identified grain crushing as the dominant micromechanism of inelastic compaction in the less cemented and macroporous samples (Baud et al., 2017). Their results were consistent with the Hertzian fracture model of Zhang et al. (1990). SML is also dominantly macroporous and weakly cemented (Figures 1 and 2). It was, however, shown by Baud et al. (2009) in their earlier study that the onset of grain crushing P^* of this rock was much lower than the model predictions (see their Figure 15a). Figure 16c suggests that this discrepancy has little to do with the proportion of quartz in SML but is more related to the complex structure of this rock, which contains porous calcite shells and nonporous calcite grains of different shapes and sizes. We conclude therefore that our new data show that the presence of a significant proportion of secondary mineral (i.e., quartz) did not impact the mechanical strength of this porous limestone in both the brittle faulting and cataclastic flow regimes.

The difference between the conclusion drawn here and the results of the study of Rybacki et al. (2003) is likely due to two principal reasons. First, the high porosity of the SML means that that quartz grains play a relatively passive role in the deformation (deformation is simply accommodated by grain crushing in the weaker calcite grains/shells). Second, our experiments were performed at room temperature; high temperatures likely exasperate the differences between calcite and quartz due to the temperature-dependence of deformation processes such as pressure solution.

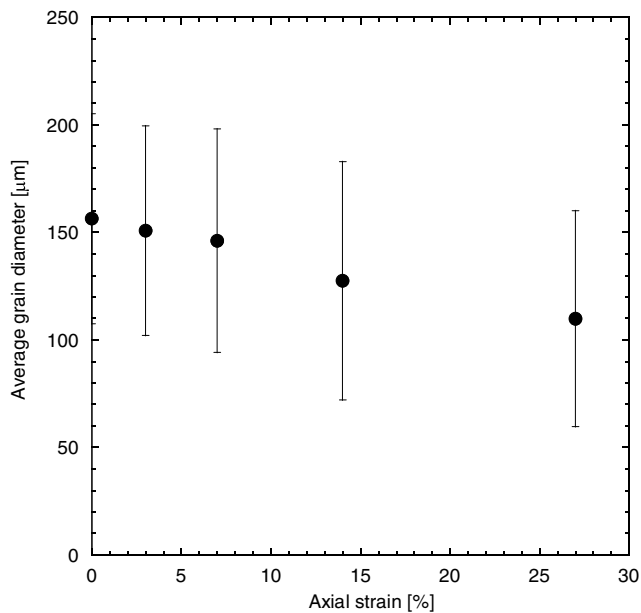


Figure 17. Quartz grain diameter in samples of Saint-Maximin limestone plotted as a function of axial strain. Samples were deformed dry under a confining pressure of 9 MPa (Figure 4a).

5.2. AE Monitoring of Damage and Compaction Localization in Porous Carbonates

Our results show that in both the brittle (Figure 16a) and ductile regimes (Figures 6–11), stress-induced damage in SML was accompanied by significant AE activity and that both the onset of dilatancy (C') and the yield point (C^*) could be identified from the AE statistics. While these results are similar to those often reported on porous sandstone (Lockner, 1993; Fortin et al., 2006, 2009a; Heap et al., 2015), previous studies on carbonates did not, to our knowledge, report consistent AE activity associated with inelastic compaction (Cilona et al., 2014; Fortin et al., 2009b; Vajdova et al., 2004). Of course, this paucity of AE data on carbonate rocks does not necessarily mean that no AE activity was recorded by previous studies but *a minima* that any AE activity, if it existed, was not significant enough to be used to monitor stress-induced damage in these rocks. In this sense, our new results on SML clearly stand out. It should, however, be noted that the number of recorded AE on SML remained relatively small with respect to what could be expected in a sandstone. To illustrate this, we deformed at EOST Strasbourg a sample of Bleurswiller sandstone of 23% porosity at an effective pressure of 80 MPa, conditions typical of the shear-enhanced compaction regime (Baud et al., 2015). All AE settings being equal to those used for sample SML64 (Figure 4b), Figure S1 in the supporting information shows that more 18 times AE energy (16 times more hits) was recorded on the sand-

stone when both rocks were deformed to 13% of inelastic strain. As a pilot study, we also deformed hydrostatically using the ENS setup, samples of Estailades (Dautriat et al., 2011), Fontvieille (Pimenta, Fortin, & Guéguen, 2014), and Indiana (Vajdova et al., 2012) limestones of porosity and 28, 24, and 16%, respectively. In contrast to the data on SML presented in this study (Figures 6 and 7), few AE events were recorded during these experiments.

These results suggest that the unusual behavior of SML could be associated to one of the particularities of this rock: the fact that it contains a significant proportion of quartz (~20 wt %). To test this hypothesis, we quantified the possible quartz grain size reduction associated with microcrack formation in sample deformed at $P_c = 9$ MPa to different levels of axial strain (Figure 4a). To do so, we manually traced around all of the quartz grains in an ~20 mm² area on a scanning electron microscopy (SEM) image of each sample and created a binary image that only showed the quartz grains. The minimum and maximum Feret diameter of each grain was determined using open source software ImageJ (the total number of grains analyzed in each image was ~200) and the equivalent grain diameter, d , was calculated using $d = \left(\frac{3}{2}\right)(d_F)$, where d_F is the average Feret diameter. These data are plotted as a function of axial strain in Figure 17. The average grain diameter of a quartz grain in the intact SML is 156 μm (Figure 17). Reductions in grain diameter were modest up to an axial strain of 7% (average grain size at 7% = 146 μm), after which grain diameter was reduced more substantially: to 127 and 110 μm at axial strains of 14% and 27%, respectively (Figure 17). These data are in line with our qualitative microstructural observations, which show that intense fracturing and grain size reduction in quartz were only observed in the samples taken to axial strains above 14% (Figures 13 and 14). However, such grain size reductions are comparatively small to those experienced by the calcite grains and fossil shells, some of which are reduced to fragments ~1 μm in diameter (Figures 13–15). Taken together, these results, coupled with the absence of any significant AE activity reported in previous studies on compaction of limestone, suggest that the origin of the intense AE activity in SML could be microcracking at the quartz grain interfaces. Future work involving experiments on synthetic quartz-calcite aggregates should be performed to confirm this conclusion.

An increasing number of experimental studies have reported compaction localization in carbonates (Arroyo, Castellanza, & Nova, 2005; Baxevanis et al., 2006; Cilona et al., 2012, 2014) but to date, the link between these results and the field examples (Tondi et al., 2006; Rustichelli et al., 2012; Rotevatn et al., 2016) remains unclear. Our new AE location data on SML show without ambiguity that compaction localization occurred in this rock. At very low effective pressure (3 MPa), the data in dry and wet conditions suggest the formation of

compactive shear bands (Bésuelle, 2001) that developed at high angle to the major principal stress (Figures 8 and 9), in agreement with our microstructural observations (Figure 14d). A similar failure mode was studied in detail on Majella limestone of 31% porosity using CT and digital image correlation by Ji et al. (2015). Due to the resolution on the location of AE hypocenters, it is not possible to compare the geometric attributes of the bands in SML with this earlier study. The AE statistics on samples SML1 and SML2 are more complex (Figures 10 and 11). The subhorizontal clusters of AE visible in Figure 10b in the sample deformed at $P_c = 9$ MPa are comparable to the compaction bands revealed using AE statistics in Bleurswiller and Diemelstadt sandstones by Fortin et al. (2006) and Townend et al. (2008), respectively. The damage pattern observed in samples SML1 deformed at $P_{eff} = 9$ MPa is, however, more similar to the results presented by Olsson and Holcomb (2000) on Castlegate sandstone of 28% porosity. The AE location data (Figure 11b) show larger clusters that move from one or both ends of the sample toward the central part. This failure mode also identified by Baud et al. (2004) in Berea and Rothbach sandstones (of 21 and 20% porosity) using quantitative microstructural analysis was named “diffuse compaction bands.” These “diffuse” bands differ from the thin discrete compaction bands observed in well-sorted sandstone (Cheung, Baud, & Wong, 2012). Our microstructural observations (Figure 12) suggest that the diffuse bands could be made of several compaction band segments. SML is a weak, poorly cemented limestone and in this sense similar to the Leitha limestone in which a recent study observed compaction bands (Baud et al., 2017). Studying samples with different cement content, they observed that increasing cementation inhibited the development of compaction localization. Since SML is more porous than their high-porosity end-member (31%), it is therefore, based on these data, quite logical to observe compaction bands in this rock. However, SML is a complex assembly of grains of different strengths: macroporous and microporous calcite shells, nonporous calcite grains, and quartz. Discrete element model simulations of Wang, Chen, and Wong (2008) showed that discrete tabular bands developed when the strength of the elements was distributed in a narrow range. We can speculate that the difference in strength of the grains composing SML could be the reason why compaction showed a more complex localized pattern in this rock.

5.3. Impact of Inelastic Compaction on Elastic Wave Velocities of Porous Carbonates

With the development of 4-D seismic monitoring in carbonate reservoirs (Grochau et al., 2014; Raef et al., 2005), a better understanding of the in situ evolution of elastic wave velocities of porous carbonates during production or CO₂ injection is clearly needed. If a significant number of laboratory studies were dedicated to the elastic wave velocities of carbonates, a large majority were performed at ambient or low pressures and focused on the effect of depositional environments and diagenesis processes (Brigaud et al., 2010), porosity (Anselmetti & Eberli, 1999; Assefa, McCann, & Sothcott, 2003), microporosity (Baechle et al., 2008; Regnet et al., 2015), or pore shape (Verwer, Braaksma, & Kenter, 2008). There is in fact a paucity of elastic wave velocity data on limestone in relation to inelastic compaction. Fortin et al. (2009b) observed a continuous decrease of the P wave velocity during hydrostatic compaction of Chauvigny limestone (17% porosity) without any significant change at the hydrostatic yielding point P^* . More recently, Regnet et al. (2015) also reported a decrease of V_p during compaction of an oolitic carbonate rock (16% porosity), but significant variations only occurred beyond the onset of cataclastic pore collapse C^* . Our new triaxial data showed a similar behavior (Figures 8–11). Since microcracking (grain crushing) was the main micromechanism of inelastic compaction at the yield point, a decrease of V_p was expected and indeed observed. The same behavior would also be expected in less porous limestones where cataclastic pore collapse (also involving microcracking) is the dominant mechanism of inelastic compaction (Vajdova et al., 2010, 2012) but, to our knowledge, no data of this nature have been published yet. Fortin et al. (2009b) argued that the different evolution observed in Chauvigny limestone as the signature of plastic pore collapse (Baud et al., 2000; Curran & Carroll, 1979), but no microstructural analysis was performed to confirm this interpretation. Our data obtained during hydrostatic compression experiments on SML (Figures 6 and 7) also showed that V_p decreased from P^* to about 3% of plastic volumetric strain, after which it increased quite rapidly. This behavior is very similar to what Fortin et al. (2007) observed in Bleurswiller sandstone: the effect of microcracking first dominated and V_p decreased near the yield point, and then the effect of porosity reduction became gradually important and started to be dominant after 3–4% of plastic volumetric strain resulting in an increase in V_p . Taken together, the published data and our new results on SML show that the variations of elastic wave velocities during inelastic compaction of limestone are to the first order dependent of the initial porosity of the rock that controls both the maximum compaction that the rock can experience and the dominant micromechanism of

inelastic compaction. An outstanding question for future studies will be to quantify in which porosity interval porous carbonates experience enough inelastic compaction to observe a significant increase in elastic wave velocities.

6. Conclusions

On the basis of our systematic investigation of the deformation and failure of SML, using rock mechanics testing, AE statistics, P wave velocity changes, and microstructural observations, we have arrived at a number of conclusions.

1. The mechanical strength of a quartz-rich limestone such as SML was not influenced by the quartz content. As in other limestones studied by previous authors (Baud et al., 2017; Baud, Wong, & Zhu, 2014; Zhu et al., 2010), microstructural attributes such as initial porosity, grain size, and pore size exert a first-order control on strength.
2. We monitored the development of stress-induced damage and strain localization using AE in SML when previous studies suggested that it was not possible in a porous limestone. Since SML stands out as an exception in this aspect, and because our quantitative microstructural analysis did not reveal extensive microcracking in quartz grains in this rock, we speculate that the recorded AE activity is likely to be due to microcracking at the interface of the quartz grains. More AE monitoring of inelastic compaction of high-porosity limestone should be performed to confirm this conclusion.
3. AE statistics and P wave velocity data revealed that compaction localization occurred in SML. However, the link between these observations and compaction bands observed in carbonate formations remains unclear.
4. Finally, our new data showed that inelastic compaction in a very porous limestone resulted first in a decrease of P wave velocity due to microcracking (grain crushing) but after a few percent of inelastic strain, the effect of compaction and pore collapse started to be dominant, resulting in an increase of P wave velocity. This behavior is very similar to previous observations on porous sandstone.

Acknowledgments

All new data included in this paper are available on the website: <https://eost.unistra.fr/recherche/ipgs/ge/ge-perso/patrick-baud/>. We thank the Associate Editor and two anonymous reviewers for thoughtful reviews. We are grateful to Bertrand Renaudié who prepared the samples in Strasbourg. We thank Emilie Walker and Candice Leforgeais who helped with some of the experiments. We have benefited from discussions with Christian David, Jamie Farquharson, Yuntao Ji, Lucas Piementa, and Teng-fong Wong.

References

- Anselmetti, F. S., & Eberli, G. P. (1999). The velocity-deviation log: A tool to predict pore type and permeability trends in carbonate drill holes from sonic and porosity or density logs. *AAPG Bulletin*, *83*, 450–466.
- Arroyo, M., Castellanza, R., & Nova, R. (2005). Compaction bands and oedometric testing in cemented soils. *Soils and Foundations*, *45*(2), 181.
- Assefa, S., McCann, C., & Sothcott, J. (2003). Velocities of compressional and shear waves in limestones. *Geophysical Prospecting*, *51*(1), 1–13. <https://doi.org/10.1046/j.1365-2478.2003.00349.x>
- Atkinson, B. K., & Meredith, P. G. (1987). Experimental fracture mechanics data for rocks and minerals. In B. K. Atkinson (Ed.), *Fracture mechanics of rock* (pp. 477–525). London: Academic Press. <https://doi.org/10.1016/B978-0-12-066266-1.50016-8>
- Aydin, A., Borja, R. I., & Eichhubl, P. (2006). Geological and mathematical framework for failure modes in granular rock. *Journal of Structural Geology*, *28*(1), 83–98. <https://doi.org/10.1016/j.jsg.2005.07.008>
- Ayling, M. R., Meredith, P. G., & Murrell, S. A. F. (1995). Microcracking during triaxial deformation of porous rocks monitored by changes in rock physical properties. I. Elastic-wave propagation measurements on dry rocks. *Tectonophysics*, *245*(3–4), 205–221. [https://doi.org/10.1016/0040-1951\(94\)00235-2](https://doi.org/10.1016/0040-1951(94)00235-2)
- Baechele, G. T., Colpaert, A., Eberli, G. P., & Weger, R. J. (2008). Effects of microporosity on sonic velocity in carbonate rocks. *The Leading Edge* (August), *27*(8), 1012–1018. <https://doi.org/10.1190/1.2967554>
- Baud, P., Meredith, P. G., & Townend, E. (2012). Permeability evolution during triaxial compaction of an anisotropic porous sandstone. *Journal of Geophysical Research*, *117*, B05203. <https://doi.org/10.1029/2012JB009176>
- Baud, P., Exner, U., Lommatzsch, M., Reuschlé, T., & Wong, T.-f. (2017). Mechanical behavior, failure mode and transport properties in a porous carbonate. *Journal of Geophysical Research: Solid Earth*, *122*, 7363–7387. <https://doi.org/10.1002/2017JB014060>
- Baud, P., Klein, E., & Wong, T.-f. (2004). Compaction localization in porous sandstones: Spatial evolution of damage and acoustic emission activity. *Journal of Structural Geology*, *26*(4), 603–624. <https://doi.org/10.1016/j.jsg.2003.09.002>
- Baud, P., Reuschlé, T., Ji, Y., Cheung, C., & Wong, T.-f. (2015). Mechanical compaction and strain localization in Bleurswiller sandstone. *Journal of Geophysical Research: Solid Earth*, *120*, 6501–6522. <https://doi.org/10.1002/2015JB012192>
- Baud, P., Rolland, A., Heap, M. J., Xu, T., Nicolé, M., Ferrand, T., ... Conil, N. (2016). Impact of Stylolites on the mechanical strength of limestones. *Tectonophysics*, *690*, 4–20.
- Baud, P., Schubnel, A., & Wong, T.-f. (2000). Dilatancy, compaction, and failure mode in Solnhofen limestone. *Journal of Geophysical Research*, *105*(B8), 19,289–19,303. <https://doi.org/10.1029/2000JB900133>
- Baud, P., Vajdova, V., & Wong, T.-f. (2006). Shear-enhanced compaction and strain localization: Inelastic deformation and constitutive modeling of four porous sandstones. *Journal of Geophysical Research*, *111*, B12401. <https://doi.org/10.1029/2005JB004101>
- Baud, P., Vinciguerra, S., David, C., Cavallo, A., Walker, E., & Reuschlé, T. (2009). Compaction and failure in high porosity carbonates: Mechanical data and microstructural observations. *Pure and Applied Geophysics*, *166*(5–7), 869–898. <https://doi.org/10.1007/s00024-009-0493-2>
- Baud, P., Wong, T.-f., & Zhu, W. (2014). Effects of porosity and crack density on compressive strength of rocks. *International Journal of Rock Mechanics and Mining Sciences*, *67*, 202–211. <https://doi.org/10.1016/j.ijrmms.2013.08.031>

- Baxevanis, T., Papamichos, E., Flornes, O., & Larsen, I. (2006). Compaction bands and induced permeability reduction in Tuffeau de Maastricht calcarenite. *Acta Geotechnica*, 1(2), 123–135. <https://doi.org/10.1007/s11440-006-0011-y>
- Bésuelle, P. (2001). Compacting and dilating shear bands in porous rocks: Theoretical and experimental conditions. *Journal of Geophysical Research*, 106(B7), 13,435–13,442. <https://doi.org/10.1029/2001JB900011>
- Bésuelle, P., Baud, P., & Wong, T.-f. (2003). Failure mode and spatial distribution of damage in Rothbach sandstone in the brittle-ductile transition. *Pure and Applied Geophysics*, 160(5), 851–868. <https://doi.org/10.1007/PL00012569>
- Brantut, N., Heap, M. J., Baud, P., & Meredith, P. G. (2014a). Mechanisms of time-dependent deformation in porous limestone. *Journal of Geophysical Research: Solid Earth*, 119, 5444–5463. <https://doi.org/10.1002/2014JB011186>
- Brantut, N., Heap, M. J., Baud, P., & Meredith, P. G. (2014b). Rate- and strain-dependent brittle deformation of rocks. *Journal of Geophysical Research: Solid Earth*, 119, 1818–1836. <https://doi.org/10.1002/2013JB010448>
- Brigaud, B., Vincent, B., Durllet, C., Deconinck, J.-F., Blanc, P., & Trouiller, A. (2010). Acoustic properties of ancient shallow-marine carbonates: Effects of depositional environments and diagenetic processes (Middle Jurassic, Paris Basin, France). *Journal of Sedimentary Research*, 80(9), 791–807. <https://doi.org/10.2110/jsr.2010.071>
- Charalampidou, E.-M., Hall, S. A., Stanchits, S., Viggiani, G., & Lewis, H. (2014). Shear-enhanced compaction band identification at the laboratory scale using acoustic and full-field methods. *International Journal of Rock Mechanics and Mining Sciences*, 67, 240–252. <https://doi.org/10.1016/j.ijmms.2013.05.006>
- Cheung, C., Baud, P., & Wong, T.-f. (2012). Effect of grain size distribution on the development of compaction localization in porous sandstone. *Geophysical Research Letters*, 39, L21302. <https://doi.org/10.1029/2012GL053739>
- Choquette, P. W., & Pray, L. C. (1970). Geologic nomenclature and classification of porosity in sedimentary carbonates. *AAPG Bulletin*, 54, 207–250.
- Cilona, A., Baud, P., Tondi, E., Agosta, F., Vinciguerra, S., Rustichelli, A., & Spiers, C. J. (2012). Deformation bands in porous carbonate grainstones: Field and laboratory observations. *Journal of Structural Geology*, 45, 137–157. <https://doi.org/10.1016/j.jsg.2012.04.012>
- Cilona, A., Faulkner, D. R., Tondi, E., Agosta, F., Mancini, L., Rustichelli, A., ... Vinciguerra, S. (2014). The effects of rock heterogeneity on compaction localization in porous carbonates. *Journal of Structural Geology*, 67, 75–93. <https://doi.org/10.1016/j.jsg.2014.07.008>
- Croizé, D., Renard, F., & Gratier, J.-P. (2013). Compaction and porosity reduction in carbonates: A review of observations, theory, and experiments. *Advances in Geophysics*, 54, 181–238. <https://doi.org/10.1016/B978-0-12-380940-7.00003-2>
- Curran, J. H., & Carroll, M. M. (1979). Shear stress enhancement of void compaction. *Journal of Geophysical Research*, 84(B3), 1105–1112. <https://doi.org/10.1029/JB084iB03p01105>
- Dautriat, J., Gland, N., Dimanov, A., & Raphanel, J. (2011). Hydromechanical behavior of heterogeneous carbonate rock under proportional triaxial loading. *Journal of Geophysical Research*, 116, B01205. <https://doi.org/10.1029/2009JB000830>
- Delle Piane, C., Burlini, L., & Kunze, K. (2009). The influence of dolomite on the plastic flow of calcite: Rheological, microstructural and chemical evolution during large strain torsion experiments. *Tectonophysics*, 467(1-4), 145–166. <https://doi.org/10.1016/j.tecto.2008.12.022>
- Eichhubl, P., Hooker, J. N., & Laubach, S. E. (2010). Pure and shear-enhanced compaction bands in Aztec sandstone. *Journal of Structural Geology*, 32(12), 1873–1886. <https://doi.org/10.1016/j.jsg.2010.02.004>
- Farquharson, J., Heap, M. J., Varley, N. R., Baud, P., & Reuschlé, T. (2015). Permeability and porosity relationships of edifice-forming andesites: A combined field and laboratory study. *Journal of Volcanology and Geothermal Research*, 297, 52–68. <https://doi.org/10.1016/j.jvolgeores.2015.03.016>
- Farquharson, J. I., Baud, P., & Heap, M. J. (2017). Inelastic compaction and permeability evolution in volcanic rock. *Solid Earth*, 8(2), 561–581. <https://doi.org/10.5194/se-8-561-2017>
- Folk, R. L. (1980). *Petrology of sedimentary rocks*. Austin: Hemphill.
- Fortin, J., Schubnel, A., & Guéguen, Y. (2005). Elastic wave velocities and permeability evolution during compaction of Bleurswiller sandstone. *International Journal of Rock Mechanics and Mining Sciences*, 42(7-8), 873–889. <https://doi.org/10.1016/j.ijmms.2005.05.002>
- Fortin, J., Schubnel, A., & Guéguen, Y. (2007). Effect of pore collapse and grain crushing on ultrasonic velocities and V_p/V_s . *Journal of Geophysical Research*, 112, B08207. <https://doi.org/10.1029/2005JB004005>
- Fortin, J., Stanchits, S., Dresen, G., & Guéguen, Y. (2006). Acoustic emission and velocities associated with the formation of compaction bands in sandstone. *Journal of Geophysical Research*, 111, B10203. <https://doi.org/10.1029/2005JB003854>
- Fortin, J., Stranchits, S., Dresen, G., & Guéguen, Y. (2009a). Acoustic emissions monitoring during inelastic deformation of porous sandstone: Comparison of three modes of deformation. *Pure and Applied Geophysics*, 166(5-7), 823–841. <https://doi.org/10.1007/s00024-009-0479-0>
- Fortin, J., Stranchits, S., Dresen, G., & Guéguen, Y. (2009b). Micro-mechanisms involved during inelastic deformation of porous carbonate rocks. In *Proceedings of the Fourth Biot Conference on Poromechanics* (pp. 378–383). New York: Columbia University.
- Fronteau, G., Moreau, C., Thomachot-Schneider, C., & Barbin, V. (2010). Variability of some Lutetian building stones from the Paris Basin, from characterisation to conservation. *Engineering Geology*, 115(3-4), 158–166. <https://doi.org/10.1016/j.enggeo.2009.08.001>
- Grgic, D., Giraud, A., & Auvray, C. (2013). Impact of chemical weathering on micro/macro-mechanical properties of oolitic iron ore. *International Journal of Rock Mechanics and Mining Sciences*, 64, 236–245. <https://doi.org/10.1016/j.ijmms.2013.09.005>
- Griggs, D. T., Turner, F. J., & Heard, H. C. (1960). Deformation of rocks at 500° to 800°C. In D. Griggs, & J. Handin (Eds.), *Rock Deformation, Memoir. Geological Society of America* (Vol. 79, pp. 39–104). <https://doi.org/10.1130/MEM79-p39>
- Grochau, M. H., Monteiro Benac, P., de Magalhães Alvim, L., Sansonowski, R. C., da Motta Pires, P. R., & Villaudy, F. (2014). Brazilian carbonate reservoir: A successful seismic time-lapse monitoring study. *The Leading Edge*, 33(2), 164–170. <https://doi.org/10.1190/le33020164.1>
- Heap, M. J., Brantut, N., Baud, P., & Meredith, P. G. (2015). Time-dependent compaction band formation in sandstone. *Journal of Geophysical Research: Solid Earth*, 120, 4808–4830. <https://doi.org/10.1002/2015JB012022>
- Ji, Y., Baud, P., Vajdova, V., & Wong, T.-f. (2012). Characterization of pore geometry of Indiana limestone in relation to mechanical compaction. *Oil & Gas Science and Technology - Revue de l'Institut Français du Pétrole*, 67(5), 753–775. <https://doi.org/10.2516/ogst/2012051>
- Ji, Y., Hall, S., Baud, P., & Wong, T.-f. (2015). Characterization of pore structure and strain localization in Majella limestone by X-ray computed tomography and digital image correlation. *Geophysical Journal International*, 200(2), 701–719. <https://doi.org/10.1093/gji/ggu414>
- Ketcham, R. A., & Carlson, W. D. (2001). Acquisition, optimization and interpretation of X-ray computed tomographic imagery: Applications to the geosciences. *Computers and Geosciences*, 27(4), 381–400. [https://doi.org/10.1016/S0098-3004\(00\)00116-3](https://doi.org/10.1016/S0098-3004(00)00116-3)
- Kushnir, A. R., Kennedy, L. A., Misra, S., Benson, P., & White, J. C. (2015). The mechanical and microstructural behaviour of calcite-dolomite composites: An experimental investigation. *Journal of Structural Geology*, 70, 200–216. <https://doi.org/10.1016/j.jsg.2014.12.006>
- Lisabeth, H. P., & Zhu, W. (2015). Effect of temperature and pore fluid on the strength of porous limestone. *Journal of Geophysical Research: Solid Earth*, 120, 6191–6208. <https://doi.org/10.1002/2015JB012152>
- Lockner, D. (1993). The role of acoustic emission in the study of rock fracture. *International Journal of Rock Mechanics and Mining Science and Geomechanics Abstracts*, 30(7), 883–899. [https://doi.org/10.1016/0148-9062\(93\)90041-B](https://doi.org/10.1016/0148-9062(93)90041-B)

- Louis, L., Wong, T.-f., Baud, P., & Tembe, S. (2006). Imaging strain localization by X-ray computed tomography: Discrete compaction bands in Diemelstadt sandstone. *Journal of Structural Geology*, 28(5), 762–775. <https://doi.org/10.1016/j.jsg.2006.02.006>
- Lucia, F. J. (1995). Rock-fabric/petrophysical classification of carbonate pore space for reservoir characterization. *AAPG Bulletin*, 79, 1275–1300.
- Menéndez, B., Zhu, W., & Wong, T.-f. (1996). Micromechanics of brittle faulting and cataclastic flow in Berea sandstone. *Journal Structural Geology*, 18, 1–16.
- Mollema, P. N., & Antonellini, M. A. (1996). Compaction bands: A structural analog for anti-mode I cracks in aeolian sandstone. *Tectonophysics*, 267(1–4), 209–228. [https://doi.org/10.1016/S0040-1951\(96\)00098-4](https://doi.org/10.1016/S0040-1951(96)00098-4)
- Nicolas, A., Fortin, J., Regnet, J.-B., Dimanov, A., & Guéguen, Y. (2016). Brittle and semi-brittle behaviours of carbonate rock: Influence of water and temperature. *Geophysical Journal International*, 206(1), 438–456. <https://doi.org/10.1093/gji/ggw154>
- Olsson, W. A., & Holcomb, D. J. (2000). Compaction localization in porous rock. *Geophysical Research Letters*, 27(21), 3537–3540. <https://doi.org/10.1029/2000GL011723>
- Ougier-Simonin, A., Fortin, J., Guéguen, Y., Schubnel, A., & Bouyer, F. (2011). Cracks in glass under triaxial conditions. *International Journal of Rock Mechanics and Mining Sciences*, 49(1), 105–121.
- Pimenta, L., Fortin, J., & Guéguen, Y. (2014). Investigation of elastic weakening in limestone and sandstone from moisture adsorption. *Geophysics*, 199(1), 335–347.
- Raef, A. E., Miller, R. D., Franseen, E. K., Byrnes, A. P., Watney, W. L., & Harrison, W. E. (2005). 4D seismic to image a thin carbonate reservoir during a miscible CO₂ flood: Hall-Gurney Field, Kansas, USA. *The Leading Edge*, 24(5), 521–526. <https://doi.org/10.1190/1.1926811>
- Rath, A., Exner, U., Tschegg, C., Grasmann, B., Laner, R., & Draganits, E. (2011). Diagenetic control of deformation mechanisms in deformation bands in a carbonate grainstone. *AAPG Bulletin*, 95(8), 1369–1381. <https://doi.org/10.1306/01031110118>
- Regnet, J. B., David, C., Fortin, J., Robion, P., Makhloufi, Y., & Collin, P. Y. (2015). Influence of microporosity distribution on the mechanical behavior of oolitic carbonate rocks. *Geomechanics for Energy and the Environment*, 3, 11–23. <https://doi.org/10.1016/j.gete.2015.07.002>
- Regnet, J. B., Robion, P., David, C., Fortin, F., Brigaud, B., & Yven, B. (2015). Acoustic and reservoir properties of microporous carbonate rocks: Implication of micrite particle size and morphology. *Journal of Geophysical Research: Solid Earth*, 120, 790–811. <https://doi.org/10.1002/2014JB011313>
- Rotevatn, A., Thorsheim, E., Bastesen, E., Fossmark, H. S. S., Torabi, A., & Saelen, G. (2016). Sequential growth of deformation bands in carbonate grainstones in the hangingwall of an active growth fault: Implications for deformation mechanisms in different tectonic regimes. *Journal of Structural Geology*, 90, 27–47. <https://doi.org/10.1016/j.jsg.2016.07.003>
- Rustichelli, A., Tondi, E., Agosta, F., Cilona, A., & Giorgioni, M. (2012). Development and distribution of bed-parallel compaction bands and pressure solution seams in the Bolognano Formation carbonates (Majella Mountain, Italy). *Journal of Structural Geology*, 37, 181–199. <https://doi.org/10.1016/j.jsg.2012.01.007>
- Rybacki, E., Paterson, M. S., Wirth, R., & Dresen, G. (2003). Rheology of calcite-quartz aggregates deformed to large strain in torsion. *Journal of Geophysical Research*, 108(B2), 2089. <https://doi.org/10.1029/2002JB001833>
- Sammis, C. G., & Ashby, M. F. (1986). The failure of brittle porous solids under compressive stress states. *Acta Metallurgica*, 34(5), 11–26.
- Schubnel, A., Walker, E., Thompson, B. D., Fortin, J., Guéguen, Y., & Young, R. P. (2006). Transient creep, aseismic damage and slow failure in Carrara marble deformed across the brittle-ductile transition. *Geophysical Research Letters*, 33, L17301. <https://doi.org/10.1029/2006GL026619>
- Tondi, E., Antonellini, M. A., Aydin, A., Marchegiani, L., & Cello, G. (2006). The role of deformation bands, stylolites and sheared stylolites in fault development in carbonate grainstones of Majella Mountain, Italy. *Journal of Structural Geology*, 28(3), 376–391. <https://doi.org/10.1016/j.jsg.2005.12.001>
- Townend, E., Thompson, B. D., Benson, P. M., Meredith, P. G., Baud, P., & Young, R. P. (2008). Imaging compaction band propagation in Diemelstadt sandstone using acoustic emission locations. *Geophysical Research Letters*, 35, L15301. <https://doi.org/10.1029/2008GL034723>
- Turner, F. J., Griggs, D. T., & Heard, H. C. (1954). Experimental deformation of calcite crystals. *Geological Society of America Bulletin*, 65(9), 883–954. [https://doi.org/10.1130/0016-7606\(1954\)65%5B883:EDOC%5D2.0.CO;2](https://doi.org/10.1130/0016-7606(1954)65%5B883:EDOC%5D2.0.CO;2)
- Ulusay, R., & Hudson, J. A. (2007). International Society for Rock Mechanics, *The complete ISRM suggested methods for rock characterization, testing and monitoring: 1974–2006*. International Soc. for Rock Mechanics, Commission on Testing Methods.
- Vajdova, V., Baud, P., & Wong, T.-f. (2004). Compaction, dilatancy, and failure in porous carbonate rocks. *Journal of Geophysical Research*, 109, B05204. <https://doi.org/10.1029/2003JB002508>
- Vajdova, V., Baud, P., Wu, L., & Wong, T.-f. (2012). Micromechanics of inelastic compaction in two allochemical limestones. *Journal of Structural Geology*, 43, 100–117. <https://doi.org/10.1016/j.jsg.2012.07.006>
- Vajdova, V., Zhu, W., Chen, T.-M. N., & Wong, T.-f. (2010). Micromechanics of brittle faulting and cataclastic flow in Tavel limestone. *Journal of Structural Geology*, 32(8), 1158–1169. <https://doi.org/10.1016/j.jsg.2010.07.007>
- Verwer, K., Braaksma, H., & Kenter, J. (2008). Acoustic properties of carbonates: Effects of rock texture and implications for fluid substitution. *Geophysics*, 73(2), B51–B65. <https://doi.org/10.1190/1.2831935>
- Wang, B., Chen, Y., & Wong, T.-f. (2008). A discrete element model for the development of compaction localization in granular rock. *Journal of Geophysical Research*, 113, B03202. <https://doi.org/10.1029/2006JB004501>
- Wang, X.-Q., Schubnel, A., Fortin, J., Guéguen, Y., & Ge, H.-K. (2013). Physical properties and brittle strength of thermally cracked granite under confinement. *Journal of Geophysical Research: Solid Earth*, 118, 6099–6112. <https://doi.org/10.1002/2013JB010340>
- Wong, T.-f., & Baud, P. (2012). The brittle-ductile transition in porous rock: A review. *Journal of Structural Geology*, 44, 25–53. <https://doi.org/10.1016/j.jsg.2012.07.010>
- Wong, T.-f., David, C., & Zhu, W. (1997). The transition from brittle faulting to cataclastic flow in porous sandstone: Mechanical deformation. *Journal of Geophysical Research*, 102(B2), 3009–3025. <https://doi.org/10.1029/96JB03281>
- Zhang, J., Wong, T.-f., & Davis, D. M. (1990). Micromechanics of pressure-induced grain crushing in porous rock. *Journal of Geophysical Research*, 95(B1), 341–352. <https://doi.org/10.1029/JB095iB01p00341>
- Zhu, W., Baud, P., & Wong, T.-f. (2010). Micromechanics of cataclastic pore collapse in limestone. *Journal of Geophysical Research*, 115, B04405. <https://doi.org/10.1029/2009JB006610>